

Vector Contrastive Learning For *Pixel-Wise* Pretraining In Medical Vision

Yuting He¹ Shuo Li^{1,2,*}

¹ Dept. of BME, ² Dept. of CDS, Case Western Reserve University, US, Cleveland

{yuting.he4, shuo.li11}@case.edu

code: <https://github.com/YutingHe-list/COVER>

Abstract

Contrastive learning (CL) has become a cornerstone of self-supervised pretraining (SSP) in foundation models; however, extending CL to pixel-wise representation—crucial for medical vision—remains an open problem. Standard CL formulates SSP as a binary optimization problem (binary CL) where the excessive pursuit of feature dispersion leads to an “over-dispersion” problem, breaking pixel-wise feature correlation thus disrupting the intra-class distribution. Our vector CL reformulates CL as a vector regression problem, enabling dispersion quantification in pixel-wise pretraining via modeling feature distances in regressing displacement vectors. To implement this novel paradigm, we propose the **CO**ntrast in **VE**ctor **RE**gression (**COVER**) framework. COVER establishes an extendable vector-based self-learning, enforces a consistent optimization flow from vector regression to distance modeling, and leverages a vector pyramid architecture for granularity adaptation, thus preserving pixel-wise feature correlations in SSP. Extensive experiments across 8 tasks, spanning 2 dimensions and 4 modalities, show that COVER significantly improves pixel-wise SSP, advancing generalizable medical visual foundation models.

1. Introduction

Contrastive learning (CL) [7, 11–13, 19, 51, 66] has become a cornerstone of self-supervised pretraining (SSP) [43] in medical visual foundation models (MVFMs) [10, 28, 47, 71, 78, 85]. However, applying CL in a *pixel-wise* manner, an approach pivotal for disentangling the clinically critical semantics within medical images [83], remains an open problem. Current preliminary works [10, 71, 78] adopt image-wise contrast strategies derived from natural image studies [11–13, 19, 51], which emphasize global representations [76]. In medical images, the global context is often similar due to the consistent anatomies in human body

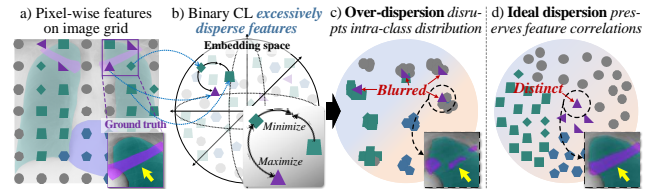


Figure 1. **Over-dispersion problem:** Binary CL excessively pursues to disperse features, disrupting intra-class distribution and struggling models to disentangle the underlying semantics.

[48], leading to a lack of global diversity that will cause CL models to converge to trivial solutions [60, 74]. Recent evidence highlights the critical importance of local features [42, 76, 80, 83] and leading results [21, 56, 81] in medical images increasingly incorporate pixel-wise methods. This observation raises a fundamental question: *Can CL be reformulated as a truly pixel-wise SSP for MVFMs?*

An obstacle to answering this question is the *over-dispersion problem* [30, 60, 74]. The standard CL formulates the SSP as a binary optimization problem (termed *binary CL*), where feature distances in positive or negative pairs are directly minimized or maximized [50], leading to excessive dispersion of features without degree modeling (Fig.1-b). However, recent findings indicate that excessive pursuit of dispersion will disrupt intra-class distribution [72, 74]. This rigid contrast imposes significant limitations on medical vision tasks that require high sensitivity to subtle variations and structures, like thin vessels and subtle lesions, which risk being blurred or indistinguishable (Fig.1-c). While some attempts [8, 79] softened the contrast or introduced regularization [74] to mitigate this problem, they remain fundamentally reliant on the binary CL.

In pixel-wise pretraining, the over-dispersion problem renders the binary CL particularly ineffective (Fig.1 a-c). Pixel-wise features are distributed across the image grid, where semantics vary continuously [18], making them inherently correlated. Unlike discrete classification tasks, continuous signals lack a natural definition of distinct categories [22, 65], leading to ambiguity near proximity divisions. The excessive pursuit of dispersion breaks these

*Corresponding author: shuo.li11@case.edu

correlations so that it aggravates the disruption of the inherent intra-class distribution, struggling pretrained models to disentangle the underlying semantics hidden in pixels [3].

Motivation: Modeling distances for pixel-wise features is essential to quantify their dispersion degrees. The binary CL follows a max-min contrast for feature distances, neglecting explicit quantification of dispersion (Fig.1-b). Ideally, suppose we can predefine a ground truth distance α to indicate the desired feature dispersion, the model will be trained to align feature distances accordingly [63, 82]. Such a CL with explicit distance modeling would enable precise quantification of dispersion while preserving feature correlations (Fig.1-d). Unfortunately, in practice, these ground truth distances are task-dependent [55], making them unmeasurable in the SSP and mismatched with the general objectives of foundation models [4].

This paper proposes a solution for the over-dispersion problem in pixel-wise CL by formulating a *vector contrastive learning*. The key insight is that feature distances inherently encode semantic correspondences and can be represented as displacement vectors in image space (Fig.2). When pixel-wise features align on an image grid, such vectors (pointing from source to target coordinates) provide a structured way to model correspondences. Therefore, instead of directly minimizing $|\alpha - d'|$ to model distances d' in the embedding space, we formulate a function \mathcal{V} that relates distances to vectors v' in the image space. This reformulates the CL as a vector regression problem: $|v - \mathcal{V}(d')|$ (formulated in Sec.3.1), where v is the ground truth vector. By leveraging the properties of vectors, this approach structurally regulates feature dispersion, preserving semantic continuity. Incorporating measurable magnitudes and directions from the image space, vector CL provides a principled way to guide CL with distance modeling.

The implementation of vector CL remains unexplored, hindered by two questions: Q1. How to construct a self-learning paradigm with free ground truth vector v that can be extended across diverse medical images? Q2. How to formulate the function \mathcal{V} to ensure a consistent optimization flow from vector regression to distance modeling while aligning with the properties of correspondence? Although preliminary studies [26, 29] explored vectors in medical SSP, they lacked a structured formulation to link distances and vectors, causing inconsistent optimization flows. *For the first time*, we formulate the vector CL and implement it as a **CO**ntrast in **VE**ctor **R**egression (**COVER**) framework, which models distance in pixel-wise CL, enabling quantitative dispersion in pixel-wise SSP via three key innovations:

1) *Self-Vector Regression (SeVR) (for Q1)* constructs an *extendable* self-space transformation mechanism for vector CL with free ground truth vectors v (Fig.3-a, Sec.3.2). Specifically, it generates a displacement vector field (DVF), a dense field of vectors on the image grid, capturing pixel-

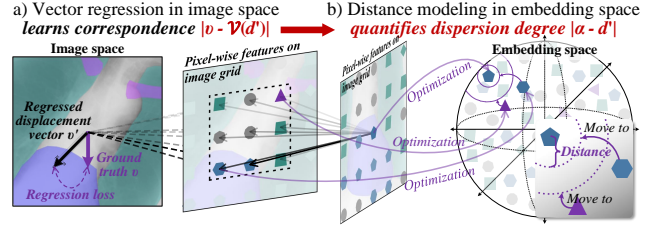


Figure 2. **Motivation:** Our vector CL unifies the distance modeling $|d - d'|$ and displacement vector regression $|v - \mathcal{V}(d')|$, enabling CL with quantitative dispersion via the optimization flow.

wise correspondences between two transformed views of a medical image. The pixel-wise distances are modeled through vector regression supervised by the DVF. This synthesis-based process enables a scalable and annotation-free SSP algorithm, facilitating vector CL across a wide variety of medical images (free from paired images [26, 29]).

2) *Mixture of Vectors (MoV) (for Q2)* formulates a mapping function with consistent optimization flow from vector regression to distance modeling (Fig.3-b, Sec.3.3) with two properties: *i. Spatial continuity.* It designs a vector embedding unit (VEU) that encodes continuous spatial relationships in a vector template to map pixel-wise feature distances to vectors, thus avoiding the artificial division [42, 76, 80] and preserving the feature correlation. *ii. Correspondence ambiguity.* It constructs a multi-vector integration (MVI) strategy that extracts multiple vectors indicating potential correspondences with diverse feature concerns, enhancing bias adaptability for pretrained models.

3) *Vector Pyramid Aggregation (VPA) (for Q2)* formulates *multiscalar*ity of correspondence via stacking the MoV in a pyramid-like architecture (Fig.3-c, Sec.3.4). It predicts vectors across multiple feature scales and fuses them to capture correspondences for semantic objects at varying scale levels. Therefore, it enables the vector CL on different scales with low computation cost, training the model to represent multiscale features and improving granularity adaptability for pretrained models.

Our contributions are summarized as follows: 1) For the first time, we pioneer a novel CL paradigm, vector CL, overcoming the over-dispersion problem in standard binary CL while preserving intra-class distribution. 2) We propose the COVER framework, which implements the vector CL for an extendable pixel-wise SSP in MVFMs. 3) Our SeVR establishes a versatile self-learning paradigm extendable across diverse medical images. 4) Our MoV maps feature distances as vectors, enabling a consistent optimization flow that quantifies dispersion while maintaining feature correlations. 5) Our VPA captures multiscale correspondences, enhancing representations across varying granularity scales.

2. Related works

1) Medical image self-supervised pretraining [43] (SSP), as a training algorithm without annotation, is effectively promoting the programming of medical visual foundation models [10, 28, 47, 85]. It will capture the posterior distribution of the underlying explanatory factors and make models easier to extract useful information [3], thus achieving the general application goal. It always utilizes the generative learning (GL) [40, 53, 70, 86] or contrastive learning (CL) [7, 11, 12, 19, 42, 51, 66, 76, 80] paradigms that train model by generating generate meaningful information or contrasting feature pairs. In this paper, we limit our scope to medical visual CL and review the below topics that are relevant to the applications considered in the sequel.

2) Binary contrastive learning has become a dominant SSP paradigm that learns general representations without annotations. Early works [11, 19, 22] maximize the distance between positive pairs while minimizing distance with negatives, leveraging global representations in natural images and being implemented to medical images [10, 71, 78]. However, the lack of global diversity in medical images makes the global representations insufficient, causing model collapse [60, 74]. While dense binary CL [76, 80] learns dense representations for local features, it suffers from *over-dispersion problem* due to mini-max dispersion, distorting their correlations and intra-class distributions [72, 74].

3) Distance modeling [63, 82] quantifies features’ distances in embedding spaces, preserving their correlations. It focuses on learning similarity metrics and guiding feature alignment with specific distance [31, 62]. This approach aligns closely with human cognition in perceiving continuous objects [15]. This has proven valuable in capturing feature correlations for effective pixel-wise feature representation. However, when aiming for SSP with general representations, predefined distances become impractical [55], posing challenges to direct distance modeling.

4) Vector regression was originally developed to learn correspondence vectors of visual objects, and has been widely applied in image registration [1, 23, 27, 73], geometric matching [16, 17, 58], etc. Some preliminary SSP works [40, 87] attempt to establish absolute correspondence between semantics and positions but overlook their relative variations. GVSL [26] and GEMINI [29] introduce correspondence learning into medical SSP by predicting vector fields that represent the dense correspondence between objects across images. However, the lack of a formulation for the mapping function between feature distances and vectors has limited its ability to exert control over pixel-wise representations. This paper addresses this gap by formulating the relationship between feature distances and their vectors.

3. COVER: COntrast in VECtor Regression

Our COVER (Fig.3) implement the formulated vector CL (Sec.3.1) via establishing the consistent optimization flow between distance modeling and vector regression (MoV, Sec.3.3), modeling multi-scale representation (VPA, Sec.3.4), and learning the vector regression in a self-learning pipeline (SeVR, Sec.3.2), thus yielding pixel-wise pretraining with quantitative dispersion in medical vision.

3.1. Formulation

3.1.1 Problem formulation The proposed vector CL reformulated the CL as a vector regression problem that models pixel-wise feature distances to quantify their dispersion degrees. It defines a mapping function \mathcal{V} that links pixel-wise features to displacement vectors with a consistent optimization flow. Given an input medical image x from dataset \mathcal{D} , we apply a random spatial transformation function \mathcal{T}_{sp} to generate two augmented views x_a, x_b with their spatial correspondence encoded in a displacement vector field (DVF) $\psi_{ab} = \{v^i\}_{i \in \Omega}$ (Ω is the image grid), where v^i represents the coordinate shift from x_a to x_b at pixel i . The network \mathcal{N}_θ extracts dense feature maps $F_a = \mathcal{N}_\theta(x_a)$ and $F_b = \mathcal{N}_\theta(x_b)$. The function \mathcal{V} then predicts the DVF $\psi'_{ab} = \{v'^i\}_{i \in \Omega}$ from these features, aiming to minimize the disparity between ψ'_{ab} and ψ_{ab} . This is formulated as:

$$\min_{\theta} \mathbb{E}_{x \sim \mathcal{D}} [|\psi'_{ab} - \psi_{ab}|], \quad (1)$$

where $\psi'_{ab} = \mathcal{V}(F_a, F_b)$, $\psi_{ab} \sim \mathcal{T}_{sp}$, $\psi_{ab}(x_a) \equiv x_b$.

The \equiv means both sides have consistent space.

3.1.2 Why does our vector CL drive distance modeling? Because the vector CL unifies feature distance modeling and displacement vector regression mathematically. It constructed an equivalency of vector regression and distance modeling, obtaining a consistent optimization flow, and thus enabling the ability to learn feature distances in the embedding space without ground truth distances. This process is formalized as follows:

$$Dist. Mod.: \sum_{i=0}^I |\alpha^i - d^i| \rightarrow 0 \quad (2)$$

$$\Leftrightarrow \sum_{i=0}^I \mathbb{V}^i |\alpha^i - d^i| \rightarrow 0 \quad (3)$$

$$\Rightarrow |\sum_{i=0}^I \mathbb{V}^i \alpha^i - \sum_{i=0}^I \mathbb{V}^i d^i| \rightarrow 0 \quad (4)$$

$$Vec. Reg.: \Leftrightarrow |v - \sum_{i=0}^I \mathbb{V}^i d^i| \rightarrow 0. \quad (5)$$

The ideal distance modeling in a set can be formulated as Equ.2, where the α^i is the ground truth distance for feature pair i in the set with I distances. Our COVER defines this distance set as the distances on a field of the image grid (Sec.3.3) and embeds a vector template matrix \mathbb{V} to weight them for Equ.3 which is equivalent with Equ.2. Based on this, Equ.4 can be deduced that illustrates when the individual distance approaches its certain value, the whole will

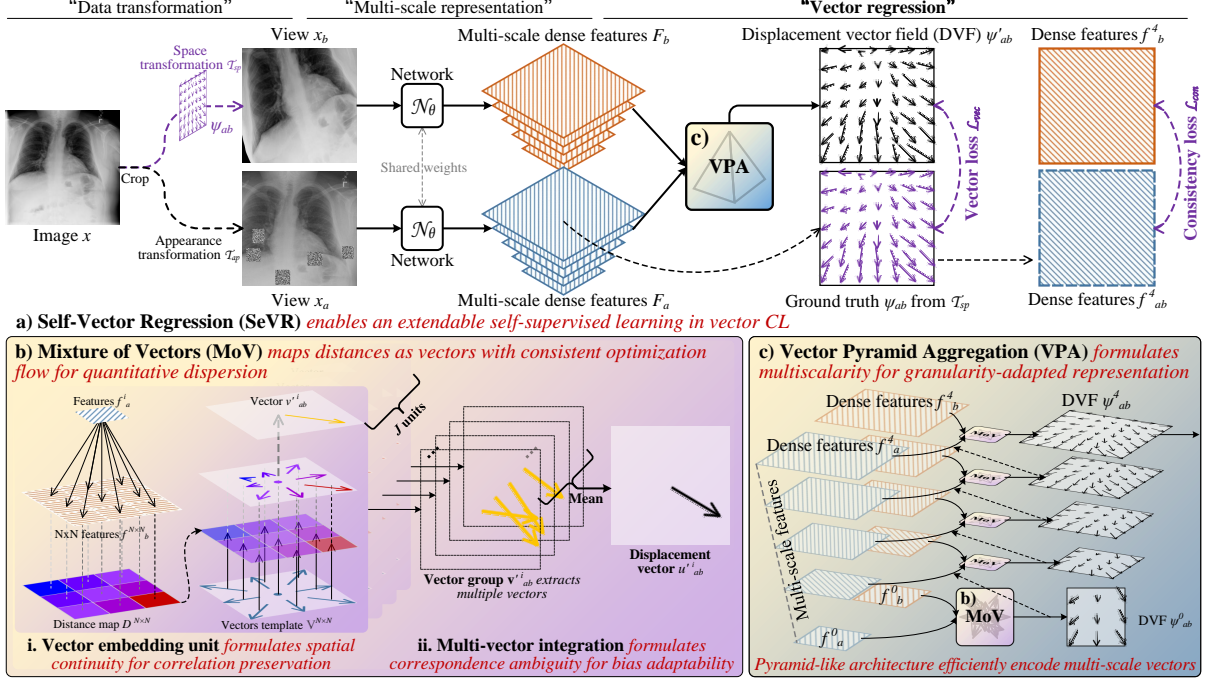


Figure 3. **Framework:** Our COVER formulates the distance modeling as the regression of displacement vectors (coordinate correspondences), quantifying dispersion degree in pixel-wise CL. a) SeVR (Sec.3.2) implements vector CL in a self-space transformation process. b) MoV (Sec.3.3) formulates feature distances as vectors with the properties of spatial continuity (VEU (i)) and correspondence ambiguity (MVI (ii)). c) VPA (Sec.3.4) formulates multiscale of correspondence via integrating the multi-scale vectors for granularity adaptability.

also approach the certain whole. Therefore, our COVER hypothesizes that existing a value v (i.e., vector in DVF ψ_{ab}) can make $\sum_{i=0}^I \mathbb{V}^i \alpha^i = v$, the Equ.5 will be derived from Equ.4, formulating distance modeling in vector regression. Compared with the binary CL, our vector CL makes a tighter generalization bound [46]. We have formulated and analyzed the theory foundations in the *supplementary*).

Equivalency of vector regression and distance modeling.

While vector regression is not strictly equivalent to conventional distance modeling, our approach of capturing overall distance distribution enhances representation generalizability. Although Equ.4 shows that the aggregated weighted error tends to zero, it does not guarantee that each individual error in Equ.3 vanishes. Fortunately, since the ground truth distance α^i is task-dependent [55], our approach captures the overall distance distribution rather than enforcing exact matches for each feature pair. This flexibility allows the model to accommodate varying feature biases across different tasks, promoting a more adaptable representation.

3.2. Self-vector regression for extendable self-learning

Our SeVR (Fig.3-a) constructs and regresses the ground truth vector v in a self-space transformation mechanism. Given a set of medical images \mathcal{D} , an image x is randomly sampled and cropped $x \sim \mathcal{D}$, and two transformation operations for appearance $t \sim \mathcal{T}_{ap}$ and space $\psi_{ab} \sim \mathcal{T}_{sp}$ are sampled for appearance and space transformation functions

$\mathcal{T}_{ap}, \mathcal{T}_{sp}$. Especially, the space transformation operation is a DVF ψ_{ab} which transforms the space of the image x and will play as the ground truth vectors $\{v^i\}_{i \in \Omega}$ in the field. Our COVER produces the transformation operations for the image x and generates two views $x_a = t(x), x_b = \psi_{ab}(x)$ with different space and appearance features. Two share-weighted networks \mathcal{N}_θ extract the pixel-wise features with L scale levels $F_a = \{f_a^l\}_{l=0}^L = \mathcal{N}_\theta(x_a), F_b = \{f_b^l\}_{l=0}^L = \mathcal{N}_\theta(x_b)$ from these views for multi-scale representation. A function $\mathcal{V}(\cdot, \cdot)$ (VPA, Sec.3.4) formulates the relationship between the distances of these features F_a, F_b , predicting the DVF ψ'_{ab} which indicates their correspondences.

Our COVER learns to regress the vector indicates the correspondence to drive the distance modeling, so a vector loss \mathcal{L}_{vec} calculates a mean absolute error between the predicted ψ'_{ab} and the ground truth DVF ψ_{ab} , i.e.,

$$\mathcal{L}_{vec}(\psi_{ab}, \psi'_{ab}, \epsilon_{ab}) = \sum_{i \in \{\epsilon_{ab}=1\}} |\psi_{ab}^i - \psi'_{ab}^i|, \quad (6)$$

where the ϵ_{ab} is a mask that eliminates the content mismatch of two views x_a, x_b caused by the spatial transformation and is generated from the ground truth DVF ψ_{ab} . It enables the network to model the correspondence degrees between one feature and a set of features (illustrated in Sec.3.3) for position correspondence, i.e., vectors. An additional consistency loss \mathcal{L}_{con} is used to maintain the invariance of semantics in space transformation. It calculates a cosine similarity between the dense features from two views, i.e.,

$\mathcal{L}_{con}(f_{ab}^4, f_b^4, \epsilon_{ab}) = -\sum_{i \in \{\epsilon_{ab}=1\}} \frac{f_{ab}^{4,i} \cdot f_b^{4,i}}{\|f_{ab}^{4,i}\| \|f_b^{4,i}\|}$, where the $f_{ab}^4 = \psi_{ab}(f_a^4)$ is the transformed 4th level dense features f_a^4 for a consistent space of dense feature f_b^4 .

The whole optimization of our COVER iteratively minimizes the $\arg \min_{\theta} \mathcal{L}_{COVER} = \mathcal{L}_{con} + \mathcal{L}_{vec}$ for weights θ . If it utilizes the SGD, its dynamics can be formulated as $\theta^* \leftarrow \theta - \eta \frac{\partial \mathcal{L}_{COVER}(\theta, \mathcal{D}, \mathcal{T}_{sp}, \mathcal{T}_{ap})}{\partial \theta}$, where the η is the learning rate. More details are illustrated in *Supplementary*.

Discussion of properties Our SeVR constructs a self-space transformation mechanism, enabling an *extendable* self-supervised learning paradigm. It generates DVFs from random transformation as the ground truth vectors v to drive the vector regression without annotation or externally paired data [26, 29]. This property makes it extendable to a wide variety of medical images for large-scale training simplifying data preparation and enhancing generality.

3.3. Mixture of vectors with consistent optimization flow

As a part of the function \mathcal{V} , our mixture of vectors (MoV, Fig.3-b) \mathcal{M} maps distances as vectors with consistent optimization flow. It constructs a vector embedding unit (VEU, b-i) and a multi-vector integration (MVI, b-ii) to encode the *spatial continuity* and *correspondence ambiguity*:

Vector embedding unit (VEU) $\mathcal{U}(\cdot, \cdot)$ For a receptive field with $N \times N$ size¹ on position i of image grid, the distances between the center feature f_a^i (from view x_a) and the set of features $f_b^{N \times N} = \{f_b^{(n,n)}\}_{n=0}^N$ in the receptive field (from view x_b) are calculated. Inspired by the attention in transformer [69], it uses the scaled dot-product attention to model their similarity to (0,1) thus achieving a distance map $D^{N \times N}$. To map the feature distances as vectors, we design a fixed vector template matrix $\mathbb{V}^{N \times N} = \{\mathbb{V}^{(n,n)}\}_{n=0}^N$ that indicates the vectors in which the center coordinate pointing to the coordinates in the receptive field. This vector template $\mathbb{V}^{N \times N}$ is matrix multiplied with the distance map $D^{N \times N}$ for a vector v_{ab}^i . The function of our VEU $\mathcal{U}(\cdot, \cdot)$ is

$$v_{ab}^i = \mathcal{U}(f_a^i, f_b^{N \times N}) = \text{softmax}\left(\frac{f_a^i f_b^{T \times N \times N}}{\tau}\right) \mathbb{V}^{N \times N}, \quad (7)$$

where the τ is a scaling factor ($\tau = \sqrt{c_k}$ in experiment following [69]). The predicted vector v_{ab}^i is the displacement of feature f_a^i to align the most similar features in $f_b^{N \times N}$.

Multi-vector integration (MVI) Our MVI predicts and integrates multiple vectors to adapt the ambiguous correspondence in a region with continuous semantics caused by varied feature concerns. The features f_a, f_b with C channels are divided into J groups, and each group is produced by our VEU \mathcal{U} for a potential vector $v^j = \mathcal{U}(f_a[j], f_b[j])$ where j is the index of group, thus achieving a vector group $\mathbf{v}' = \{v^j\}_j^J$ representing the correspondences in different feature concerns. Finally, it averages the vectors in the

¹For a clearer illustration, we take 2D situation as example.

group for a displacement vector $u' = \frac{1}{J} \sum_{j=0}^J v^j$ that is compatible with the ambiguity of correspondence. Calculating the displacement vectors for all positions on the image grid, our MoV will output the displacement vector field (DVF) $\psi'_{ab} = \{u_{ab}^i\}_{i \in \Omega}$ that indicates the correspondence of dense features between view x_a and x_b .

Discussion of properties Our MoV constructs a consistent optimization flow from vector regression to distance modeling to quantify the dispersion. It encodes the properties of *spatial continuity* and *correspondence ambiguity* of the pixel-wise features, bringing two advantages: 1) *Feature correlation preservation*: Our VEU constructs a vector template \mathbb{V} that describes this continuous spatial relationship. This template \mathbb{V} maps the feature distances to vectors that avoid the artificial division [42, 76, 80] thus preserving the feature correlation. 2) *Bias adaptability*. Pixel-wise correspondence is uncertain and task-dependent, our MVI models this ambiguity to represent diverse feature concerns, enhancing bias adaptability in general applications.

3.4. Vector pyramid aggregation adapts granularity

Stacking our MoV \mathcal{M} in a pyramid-like architecture, our vector pyramid aggregation (VPA, Fig.3-c) formulates the final mapping function \mathcal{V} to model the multiscale of correspondence efficiently, training a granularity adaptability. This architecture divides multi-level correspondences according to the scale levels of the dense features. By fusing these scale levels, the VPA will output the DVF ψ'_{ab} that models both global and local correspondences. In 0th level, dense features f_a^0, f_b^0 are put into our MoV module for a 0th-level DVF $\psi_{ab}^0 = \mathcal{M}(f_a^0, f_b^0)$ with a global correspondence for high-level features. Then, in 1st level, the ψ_{ab}^0 transforms the 1st-level dense features f_a^1 to bridge the space gap between f_a^1 and f_b^1 on the 0th level. The features are further produced by our MoV and further fused with the ps_{ab}^i for the 1st-level DVF $\psi_{ab}^1 = \mathcal{M}(\psi_{ab}^0(f_a^1), f_b^1) \odot \psi_{ab}^0$, where the “ \odot ” is the fusion operation illustrated in *Supplementary*. The remaining levels are calculated similarly so that the final DVF ψ'_{ab} integrated multiscale vectors are output after a chain calculation, i.e.

$$\begin{aligned} \psi'_{ab} &= \mathcal{V}(F_a, F_b) = H(\{\psi_{ab}^l\}_{l=0}^L), \text{ where} & (8) \\ \psi_{ab}^0 &= \mathcal{M}(f_a^0, f_b^0) \\ \psi_{ab}^l &= \mathcal{M}(\psi_{ab}^{l-1}(f_a^l), f_b^l) \odot \psi_{ab}^{l-1}, \quad l = 1, 2, \dots, L-1, \end{aligned}$$

where the H is the chain calculation across all L levels to output the final DVF ψ'_{ab} . Linear upsampling and value doubling are applied to bridge the scale gap of the DVFs.

Discussion of properties Correspondence occurs at multiple scales for different semantic granularity, so our VPA formulates this *multiscale* in a pyramid-like architecture, bringing the advantages: 1) *Low computational cost*: It enables the mapping function \mathcal{V} in a small receptive

Type	Methods	a) 2D evaluation pretrained on [75]				b) 3D evaluation pretrained on [45]				AVG
		SCR _S ^{25%}	PDCXR _C	KiPA22 _S ^{2D}	FIVES _S	CANDI _S	FeTA21 _S	KiPA22 _S ^{3D}	STOIC _C	Score %
-	Scratch	81.8	90.4	74.1	79.4	84.0	56.9	72.4	72.0	76.4
GL	Denosing [70]	83.9(+1.9)	92.0(+1.6)	60.3(-13.8)	77.8(-1.6)	83.7(-0.3)	52.9(-4.0)	70.0(-2.4)	65.9(-6.1)	73.3(-3.1)
	In-painting [53]	85.1(+3.3)	93.9(+3.5)	64.4(-9.7)	78.9(-0.5)	88.5(+4.5)	54.4(-2.5)	69.7(-2.7)	67.2(-4.8)	75.3(-1.1)
	Models Genesis [86]	86.1(+4.3)	92.6(+2.2)	66.6(-7.5)	79.6(+0.2)	88.7(+4.7)	55.8(-1.1)	75.8(+3.4)	75.3(+3.3)	77.6(+1.2)
	Rotation [40]	80.5(-1.3)	89.9(-0.5)	69.7(-4.4)	80.3(+0.9)	89.4(+5.4)	58.7(+1.8)	77.4(+5.0)	68.8(-3.2)	76.8(+0.4)
BCL	SimSiam [12]	87.2(+5.4)	92.2(+1.8)	72.6(-1.5)	84.3(+4.9)	87.3(+3.3)	58.7(+1.8)	83.8(+11.4)	69.5(-2.5)	79.5(+3.1)
	BYOL [19]	89.4(+7.6)	86.6(-3.8)	74.1(0)	83.3(+3.9)	89.7(+5.7)	59.2(+2.3)	83.6(+11.2)	74.0(+2.0)	80.0(+5.4)
	SimCLR [11]	89.0(+7.2)	94.7(+4.3)	74.4(+0.3)	84.5(+5.1)	89.2(+5.2)	53.4(-3.5)	78.9(+6.5)	60.7(-11.3)	78.1(+1.7)
	MoCov2 [13]	84.3(+2.5)	93.2(+2.8)	69.6(-4.5)	80.7(+1.3)	89.7(+5.7)	61.5(+4.6)	78.0(+5.6)	74.8(+2.8)	79.0(+2.6)
	DeepCluster [7]	84.0(+2.2)	93.3(+2.9)	72.7(-1.4)	81.6(+2.2)	89.8(+5.8)	57.4(+0.5)	79.7(+7.3)	65.6(-6.4)	78.0(+1.6)
DBCL	VADeR [49]	85.2(+3.4)	92.8(+2.4)	62.8(-11.3)	78.9(-0.5)	87.4(+3.4)	43.1(-13.8)	72.1(-0.3)	73.2(+1.2)	74.4(-2.0)
	DenseCL [76]	85.0(+3.2)	92.4(+2.0)	70.8(-3.3)	79.2(-0.2)	87.7(+3.7)	43.7(-13.2)	74.0(+1.6)	58.8(-13.2)	74.0(-2.4)
	SetSim [77]	85.2(+3.4)	93.9(+3.5)	70.8(-3.3)	80.1(+0.7)	88.4(+4.4)	58.7(+1.8)	73.5(+1.1)	60.1(-11.9)	76.3(-0.1)
	DSC-PM [42]	90.5(+8.7)	91.8(+1.4)	77.2(+3.1)	83.8(+4.4)	88.5(+4.5)	52.2(-4.7)	79.0(+6.6)	59.5(-12.5)	77.8(+1.2)
	PixPro [80]	91.5(+9.7)	93.0(+2.6)	73.6(-0.5)	84.3(+4.9)	89.9(+5.9)	60.7(+3.8)	80.0(+7.6)	75.1(+3.1)	81.0(+4.6)
	Chaitanya et al. [8]	87.3(+5.5)	90.0(-0.4)	76.5(+2.4)	84.9(+5.5)	87.4(+3.4)	53.4(-3.5)	70.7(-1.7)	67.8(-4.2)	77.3(+0.9)
VR	GVSL [26]	89.7(+7.9)	92.5(+2.1)	78.9(+4.8)	86.2(+6.8)	89.1(+5.1)	62.6(+5.7)	84.3(+11.9)	75.4(+3.4)	82.3(+5.9)
	GEMINI [29]	92.4(+10.6)	92.9(+2.5)	79.1(+5.0)	85.3(+5.9)	90.0(+6.0)	61.7(+4.8)	85.0(+12.6)	79.5(+7.5)	83.2(+6.8)
VCL	COVER (Ours)	94.0(+12.2)	95.9(+5.5)	80.0(+5.9)	87.2(+7.8)	89.9(+5.9)	63.6(+6.7)	85.2(+12.8)	80.4(+8.4)	84.5(+8.1)

Table 1. **Comparison study:** Our COVER achieves the best performance compared with 17 methods on 8 downstream tasks across a) 2D and b) 3D, showing our great adaptation ability. “AVG” is the average rank of the row. The blue values are the improvement compared with the “Scratch” and the bold values are the highest score. “S” and “C” are the segmentation and classification tasks.

field at each level for a large whole receptive field reducing the computation. 2) *Multi-scale representation:* It learns the multi-scale features with multiple semantic granularities improving the granularity adaptability.

4. Experiments

4.1. Comparison study

4.1.1 Experiment protocol This study has made sufficient experiments to ensure a complete evaluation. Following is the overview protocol and details are in our *Supplementary*.

1) Materials: This study evaluated our COVER across 8 tasks across 2D and 3D evaluations with 4 modalities to showcase its versatility and advantages. **a) 2D evaluation:** It pretrained networks on the ChestX-ray6 dataset [75] containing 112,120 chest X-ray images. These pretrained models are fine-tuned on four tasks (SCR_S^{25%} [68] (X-ray), PDCXR_C [37] (X-ray), FIVES_S [35] (fundus), KiPA22_S^{2D} [24] (CT)). **b) 3D evaluation:** It pretrained networks on 837 3D T1 brain MR images from the PPMI database [45]. These pretrained models are then fine-tuned to three datasets with four tasks (CANDI_S [36] (MR), FeTA21_S [54] (MR), STOIC_C [57] (CT), KiPA22_S^{3D} [24] (CT)). The evaluations involve segmentation (S) and classification (C) tasks. To evaluate the data amount robustness, it used 25% of the training set in SCR_S, and more data amount evaluations are performed in our analysis (Fig.4 b)).

2) Comparisons: This study benchmarked COVER with 17 recent or classic methods across four categories: GL [40, 53, 70, 86], binary CL (BCL) [7, 11–13, 19], dense binary CL (DBCL) [8, 42, 49, 76, 77, 80], and vector regression (VR) [26, 29]. It used 2D and 3D U-Nets [59] as the backbone \mathcal{N}_θ (for the methods with global prediction, like

MoCov2, it adopted the encoder part). For a fair comparison, full-parameter fine-tuning is employed in downstream tasks.

3) Implementation and evaluation metrics: Following [26], all tasks were implemented by PyTorch and optimized by Adam with a learning rate of 10^{-4} . The models were pretrained with 2×10^5 iterations for pretraining tasks and fine-tuned with 4×10^4 iterations for downstream tasks. Training and testing were implemented on NVIDIA A100 SXUM4 GPU with 40 GB memory. This study used the Dice coefficient (DSC) for segmentation tasks and area under curve (AUC) for classification tasks [64].

4.1.2 Quantitative analysis Our great adaptability for the downstream tasks shown in Tab. 1 demonstrates our COVER’s powerful general representation for medical vision. Two observations can be discovered:

1) Cross-scale transferability. The SOTA performances on small and large targets show our powerful cross-scale transferability owing to the learned multiscale from our VPA **a**. For small structures like the vessels (FIVES_S) and brain tissues (CANDI_S and FeTA_S), our approach achieved 87.2%, 89.9%, and 63.6% DSC with the improvements of 7.8%, 5.9%, and 6.7% over the “Scratch”. These gains stem from learning fine-grained representations at lower-scale levels. **b**. For large structures including the chest regions (SCR_S^{25%}) and kidney structures (KiPA22_S^{2D}, and KiPA22_S^{3D}), our model achieved 94.0%, 80.0%, and 85.2% DSC improving by over 5% compared to “Scratch”. This is attributed to leveraging high-scale levels for coarse-grained representation. **c**. For classification tasks (PDCXR_C and STOIC_C), our COVER achieved AUC improvements of 5.5% and 8.4% by learning global representations at level 0. Although the GVSL and GEMINI also have improvements

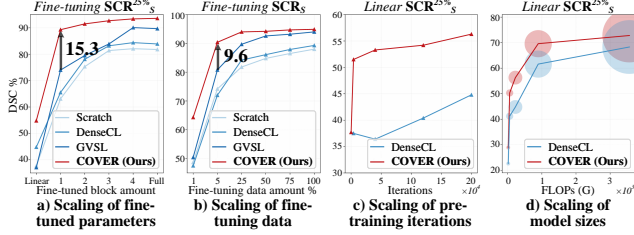


Figure 4. **Implementation analysis:** Our COVER has great properties on the scaling of a) fine-tuned parameters, b) fine-tuning data, c) pretraining iterations, and d) model sizes.

across scales, their inconsistent optimization flow limits the representation potential of pretraining data, resulting in an average score over 1% lower than COVER. The BCL methods struggle to enhance all tasks, for example, the DenseCL improved 3.2% DSC on SCR, but it reduced 3.3% DSC on KiPA22_S^{2D}. This arises from their over-dispersion, which introduces biases and compromises on incompatible tasks.

2) **Cross-scene adaptability.** The significant improvements on consistent (SCR_S^{25%}, PDCXR_C, CANDI_S) and inconsistent (KiPA22_S^{2D}, FIVES_S, FeTA_S, KiPA22_S^{3D}, STOIC_C) scenes relative to the pretraining data illustrates our strong cross-scene adaptability. Across all tasks in both 2D and 3D evaluations, COVER outperformed the “Scratch” by more than 5% and achieved the highest average scores (84.5%). This adaptability arises from our distance modeling which quantifies the dispersion in embedding space, enabling the disentanglement of underlying explanatory factors hidden in low-level sensory data [3]. These learned factors capture the intrinsic properties of medical images, enhancing versatility across diverse scenes. Although most methods improve performance in consistent scenes by leveraging learned transformable knowledge, they struggle in inconsistent scenes. Notably, BCL and DBCL even degrade performance in some tasks due to their over-dispersion in binary CL, which amplifies biases in pre-training data. Especially, DenseCL and VADeR perform particularly poorly in inconsistent scenes like FeTA21_S, which reduce over 10% DSC.

4.2. Ablation study and model analysis

4.3.1 **Component ablation** The ablation study of the components in our COVER on the 2D evaluation of SCR_S^{25%} task shows the effectiveness of our proposed innovations. This study took the learning of the consistency loss \mathcal{L}_{con} in pixel-wise as our base model, and gradually added our proposed components. The results are as follows:

	base. \mathcal{L}_{con}	...+VEU (SeVR)	...+VPA	...+MVI
DSC%	91.8	92.9	93.4	94.0

The base model \mathcal{L}_{con} has 91.8% DSC that is higher than the BYOL’s 89.4% owing to its pixel-wise representation.

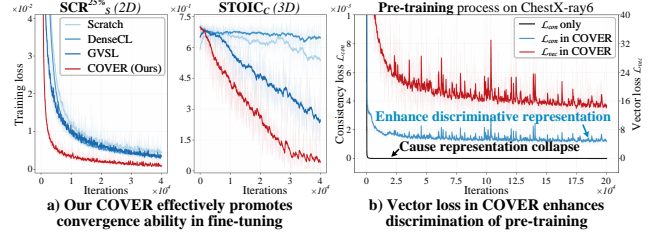


Figure 5. **Convergence analysis:** a) Our COVER is able to promote convergence ability in fine-tuning. b) In the pretraining, the consistency learning causes representation collapse, and when adding our vector regression, the discrimination is enhanced.

When adding our VEU, it effectively improves the discrimination, achieving a 1.1% improvement. Our VPA enhances the multi-scale representation so that the model further improves 0.5% DSC. Finally, our MVI models the ambiguity of the correspondence for potentially varied feature concerns, thus achieving the highest 94.0% DSC.

4.3.2 **Hyper-parameter ablation** The receptive field N in VEU, the amount of VEUs J in MVI are two new hyper-parameters in our COVER. This study took an ablation of them on the SCR_S^{25%} via *linear evaluation* to demonstrate their properties. The results are as follows:

$N =$	3×3	5×5	7×7	9×9
DSC%	44.9	48.4	54.8	35.1
$J =$	[2, 2, 2, 1, 1]	[4, 4, 4, 1, 1]	[8, 8, 8, 2, 2]	[12, 12, 12, 3, 3]
DSC%	55.3	56.3	54.8	48.6

For the receptive field size N , when enlarging it, its performance increases to 7×7 and then decreases when it is 9×9 . Because the increase of N will adapt to large spatial correspondence, improving the pretrained representation. However, too large N will introduce more ambiguous semantics, such as vascular with similar features, which will mislead the learning of correspondence. For the amount of VEUs k , it also increases and then decreases. When it is [4,4,4,1,1] for the scale levels, the model achieves the best ability. Too many vectors will smooth the optimization, thus weakening the discrimination of learned features.

4.3.3 **Implementation analysis** This experiment analyzed four implementation factors (Fig.4): a) Fine-tuned parameter amount: Our COVER effectively reduces the fine-tuned parameters. It only fine-tunes one U-Net module to achieve a very significant performance improvement (15.3% DSC higher than GVSL), quickly reaching the bottleneck level that SCR_S^{25%} task can reach. b) Fine-tuning data amount: Our COVER effectively reduces the fine-tuning data requirement. Only utilizing 5% training data, our COVER can achieve the DSC close to 90% that GVSL and DenseCL have to use 25% and 100% data. c) pretraining iteration: With the progress of the training iterations, the performance (linear evaluation) on SCR_S^{25%} of our COVER gradually improves and eventually tends to be flat. This il-

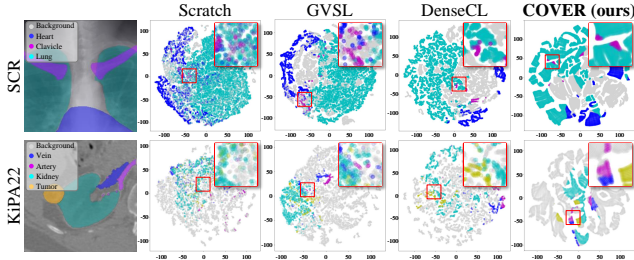
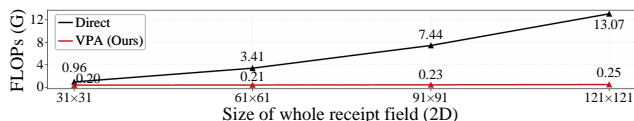


Figure 6. **Cluster analysis:** Our COVER has strong clustering capabilities by quantifying the dispersion degree of features.

illustrates that more training is beneficial for the vector CL, which makes the pretrained models capture more diverse features in detail. d) Model size: With the enlarging of model size, the larger capacity enables our COVER to capture more abundant feature information in the pretraining. This makes the model gain more powerful representability in downstream tasks only with a linear layer.

4.3.4 Convergence analysis This study analyzed the convergence performance of our COVER in both pretraining and fine-tuning phases (Fig.5): *a) Fine-tuning:* In downstream tasks, the network pretrained by our COVER exhibits superior convergence ability. Compared with the “Scratch”, GVSL, and DenseCL, COVER achieves a significantly lower loss value more quickly in both 2D segmentation (SCR) and 3D classification (STOIC) tasks. This advantage arises from our powerful pixel-wise feature learning that enables the pretrained network to capture the detailed information internal medical images. *b) pretraining:* COVER improves the discrimination of the representation. When relying solely on the consistency loss \mathcal{L}_{con} , the loss quickly collapses to zero, hindering subsequent knowledge learning. By integrating vector regression \mathcal{L}_{vec} , the model learns feature distances, stabilizing the consistency loss with fluctuations and enhancing the discrimination.

4.3.5 Computation efficiency This study calculated the FLOPs to evaluate the computation efficiency with the expanding of receptive field. For a significant analysis, we focused on the computation in head part, i.e., our VPA. It compared two methods: a. VPA; b. directly taking a large vector template at level 4 (named “Direct”). The results are:



When expanding the whole receptive field, our VPA maintains a stable computational cost of 0.2, whereas the “Direct” approach shows an exponential increase. Especially when it is 121×121 , the “Direct” has more than 52 times our consumption. Our VPA is able to expand the receptive field for a wider contrast with low additional consumption.

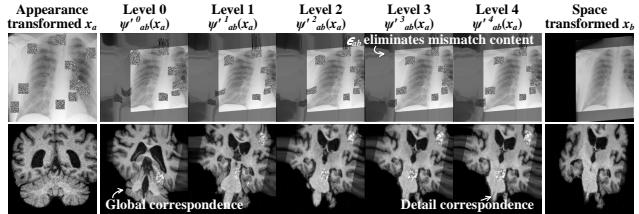


Figure 7. **Multi-scale vectors analysis:** Our VPA predicts multi-scale correspondence for both global and detailed representation.

4.3.6 Distributed clusters from COVER The clusters show that our COVER has strong clustering capabilities by quantifying the dispersion of features. Using pretrained models from our 2D evaluation, this study extracted pixel-wise features from the SCR and KiPA22 datasets and visualized their distributions via t-SNE [67] in Fig.6. It compared the clustering patterns of “Scratch”, GVSL, and DenseCL with our COVER, revealing two key advantages: a) Continuous feature distribution: Our COVER predicts features that are distributed continuously in the embedded space. This continuity arises from our vector CL, which models the feature distance and avoids the excessive discretization that blurs small or subtle features. However, DenseCL produces a lot of discrete clusters with small gaps between them, i.e., over-dispersion, leading to fragmented representation and reduced transferability. b) Effective aggregation: Our COVER aggregates features with the same semantics, while other methods show mixed regions. In both SCR and KiPA22 datasets, “Scratch” and GVSL exhibit overlapped clusters, as shown in the enlarged patches. Although DenseCL performs well on SCR, it fails on KiPA22, mixing features in this inconsistent scene with the pretraining. Our COVER achieves effective aggregation across datasets because our modeling of distance mitigates the overfitting to the pretraining scene.

4.3.7 Analysis of multi-scale vectors in our VPA This study analyzes the vectors at each scale level in our VPA by visualizing spatial transformed images via the predicted DVFs (Fig.7) in our 2D (chest X-ray) and 3D (brain MR) evaluations. In level 0, the DVF predicted from global features is able to align the images on the whole, like the rotation, scaling, etc., driving the learning of global representation. With the expansion of the scales, the correspondences are gradually refined so the details between the images are aligned. Especially, in level 0, the images have high alignment degree on the boundary, so that the models will effectively learn the representation of small or subtle features.

5. Conclusion

In this paper, we reformulate the standard CL as a vector regression problem, vector CL, providing a solution for “over-dispersion” problem caused by binary CL in pixel-wise medical visual pretraining. Our proposed **C**ontrast in

VECTOR REGRESSION (COVER) framework implemented the reformulated vector CL, modeling feature distance for CL in a vector regression process. It enables quantitative dispersion of features which improves representation learning for medical vision applications. Although the unique properties of our vector CL have bright powerful performance, important future work is to involve a larger-scale medical image dataset in training, fostering the development of a large pixel-wise foundation model in the medical field. Beyond advancing MVFM [28] development, COVER opens new frontiers in learning semantically coherent representations for continuous signals.

Acknowledgment This research was supported by the National Science Foundation grants (2306545) and National Institutes of Health grants (1R01HL177813-01, 1R01HL173186-01A1).

Supplementary Material

A. Theoretical Foundation

Existing pixel-wise contrastive learning (CL) still follows binary CL [7, 11–13, 19, 51, 66] that pulls positive pairs together and push negative pairs apart, being extremely limited by the over-dispersion problem, leading to a loss of local semantic continuity—an issue especially detrimental to medical image analysis. In contrast, we introduce a theoretical framework to derive the generalization bound for pixel-wise CL. We propose a novel CL paradigm, vector CL, which models the distances between pixel-wise features through a structured mapping function, controlling dispersion while preserving local correlations.

A.1. Recap of the Over-Dispersion Problem and Rademacher Complexity

Foundation of Contrastive Learning Let $x \in \mathcal{X}$ denote an input medical image, and assume that a network $f : \mathcal{X} \rightarrow \mathbb{R}^d$ extracts pixel-wise features $\{f(x)_i\}_{i=1}^N$ from the image, where N is the number of pixels. Define a similarity metric $\langle f_\theta(x_i), f_\theta(x_j) \rangle$ to measure the distance between pixel-wise features. In binary CL, the loss \mathcal{L}_{BCL} for a given pixel on position i can be expressed as an InfoNCE-style [50] objective:

$$\mathcal{L}_{BCL} = -\log \frac{e^{\langle f(x)_i, f(x^+)_i \rangle / \tau}}{e^{\langle f(x)_i, f(x^+)_i \rangle / \tau} + \sum_j e^{\langle f(x)_i, f(x^-)_j \rangle / \tau}}, \quad (9)$$

where x^+ is a positive (similar) view of x and x^- represents negative samples; τ is a temperature parameter. For pixel-wise tasks, we additionally assume a local smoothness constraint: for any pixel on position i and its local neighborhood $\mathcal{N}(i)$,

$$\langle f(x)_i, f(x)_j \rangle \leq \delta, \quad \forall j \in \mathcal{N}(i), \quad (10)$$

with δ being a small constant relative to the range of possible feature values Δ . The upper bound of the δ to describe the dispersion of the local features: for any two pixels on position j, k in the local neighborhood $\mathcal{N}(i)$,

$$\delta = \max_{j, k \in \mathcal{N}(i)} |\langle f(x)_i, f(x)_j \rangle - \langle f(x)_i, f(x)_k \rangle|. \quad (11)$$

Foundation of Rademacher Complexity Let \mathcal{F} denote the hypothesis space of feature extractors. The empirical Rademacher complexity [46] is defined as

$$\mathfrak{R}_n(\mathcal{F}) = \mathbb{E}_\sigma \left[\sup_{f \in \mathcal{F}} \frac{1}{n} \sum_{i=1}^n \sigma_i f(x_i) \right], \quad (12)$$

where $\{\sigma_i\}$ are independent Rademacher variables. For pixel-wise learning, one might consider nN samples (with n images and N pixels per image). However, the local smoothness constraint effectively reduces the “degrees of freedom” in each local neighborhood [2, 39]. We can thus define an effective local Rademacher complexity as

$$\mathfrak{R}_{n, \text{local}}(\mathcal{F}) \leq \left(\frac{\delta}{\Delta} \right) \mathfrak{R}_n(\mathcal{F}), \quad (13)$$

where the factor δ/Δ represents the reduction in complexity due to local smoothness.

By standard generalization theory [46], for any $f \in \mathcal{F}$, with high probability (at least $1 - \varepsilon$), the generalization error satisfies

$$R(f) \leq \hat{R}(f) + 2\mathfrak{R}_{n, \text{local}}(\mathcal{F}) + O\left(\sqrt{\frac{\log(1/\varepsilon)}{nN}}\right), \quad (14)$$

or equivalently,

$$R(f) \leq \hat{R}(f) + 2\left(\frac{\delta}{\Delta}\right)\mathfrak{R}_n(\mathcal{F}) + O\left(\sqrt{\frac{\log(1/\varepsilon)}{nN}}\right). \quad (15)$$

Thus, reducing the maximum local difference δ through better modeling of local continuity directly tightens the generalization bound.

Over-Dispersion Problem In the binary CL, since there is no explicit control over how close or dispersed feature representations are within a local neighborhood $\mathcal{N}(i)$, the difference between adjacent pixel features δ_{BCL} is unrestricted and can increase without bound. Therefore, the features will be free to spread apart as long as they satisfy the binary CL objective. This can lead to *over-dispersion*, where nearby pixels develop large feature differences, even if they belong to the same structure or object in the image. Mathematically, this means that for neighboring pixels $j \in \mathcal{N}(i)$, their feature similarity can vary widely:

$$\langle f(x)_i, f(x)_j \rangle \rightarrow \text{anywhere within } [-\Delta, \Delta], \quad (16)$$

since no term in binary CL enforces a small difference. This means binary CL lacks a mechanism to prevent large local variations, the feature differences δ_{BCL} can span the entire range of possible feature values Δ . Thus, in the worst case:

$$\delta_{BCL} \approx \Delta. \quad (17)$$

This means adjacent pixel features could be as different as features from completely unrelated image regions, which is undesirable for pixel-wise tasks like segmentation or medical image analysis. Therefore, the generalization error satisfies in the binary CL is

$$R_{BCL}(f) \leq \hat{R}(f) + 2\mathfrak{R}_n(\mathcal{F}) + O\left(\sqrt{\frac{\log(1/\varepsilon)}{nN}}\right), \quad (18)$$

causing the over-dispersion problem and limiting the generalization.

A.2. Vector Contrastive Learning

Derivation for Vector Contrastive Learning Vector CL introduces an additional regression loss that explicitly enforces the mapping between feature distances and corresponding spatial displacement vectors. Its loss is

$$\mathcal{L}_{\text{vec}} = \|v - \mathcal{V}(d')\|, \quad (19)$$

where v represents the ground-truth displacement vector and $\mathcal{V}(d')$ is a mapping function applied on the computed feature distances d' . It is formulated as a weighted sum of a vector template matrix \mathbb{V} , i.e., $\mathcal{V}(d') = \sum_{j=0}^{\mathcal{N}(i)} \mathbb{V}^j d'^j$, where the $d'^j = \frac{e^{\langle f(x)_i, f(x)_j \rangle / \tau}}{\sum_j^{\mathcal{N}(i)} e^{\langle f(x)_i, f(x)_j \rangle / \tau}}$. Therefore, the loss in vector CL \mathcal{L}_{VCL} can be further formulated as

$$\mathcal{L}_{VCL} = \left\| v - \sum_{j=0}^{\mathcal{N}(i)} \mathbb{V}^j \frac{e^{\langle f(x)_i, f(x)_j \rangle / \tau}}{\sum_j^{\mathcal{N}(i)} e^{\langle f(x)_i, f(x)_j \rangle / \tau}} \right\| \quad (20)$$

To minimize the \mathcal{L}_{VCL} , the model must adjust feature similarity $\langle f(x)_i, f(x)_j \rangle$ so that the weighted sum of \mathbb{V}^j matches v . We assume that the v can be modeled as

$$v = \sum_j^{\mathcal{N}(i)} \alpha_j \mathbb{V}^j \quad (\alpha_j \geq 0, \sum_j^{\mathcal{N}(i)} \alpha_j = 1), \quad (21)$$

the model enforces $\frac{e^{\langle f(x)_i, f(x)_j \rangle / \tau}}{Z} \approx \alpha_j$, where the $Z = \sum_j^{\mathcal{N}(i)} e^{\langle f(x)_i, f(x)_j \rangle}$. Therefore, the similarity $\langle f(x)_i, f(x)_j \rangle$ can be further approximated as

$$\langle f(x)_i, f(x)_j \rangle \approx \tau \log \alpha_j + \tau \log Z. \quad (22)$$

The maximum difference of our vector CL between any two pixels in the $\mathcal{N}(i)$ can be formulated is:

$$\begin{aligned} \delta_{VCL} &= \max_{i,k} |\langle f(x)_i, f(x)_j \rangle - \langle f(x)_i, f(x)_k \rangle| \\ &= \max_{i,k} |\tau \log \alpha_j + \tau \log Z - \tau \log \alpha_k - \tau \log Z| \\ &= \tau \max_{i,k} \left| \log \frac{\alpha_j}{\alpha_k} \right|. \end{aligned} \quad (23)$$

Owing to the $\alpha_j, \alpha_k \in [\alpha_{\min}, 1]$ ($\alpha_{\min} > 0$), when $\alpha_j = 1, \alpha(k) = \alpha_{\min}$ the δ_{VCL} will be:

$$\delta_{VCL} \leq \tau \log \frac{1}{\alpha_{\min}}. \quad (24)$$

due to the normalization of weights ($\sum_j \alpha_j = 1$), only when $\alpha_j = 1$, all other $\alpha \in \mathcal{N}(i)$ are 0. This situation where one weight is exactly 1 and all others are zero is degenerate (and would essentially revert to binary CL), so typically the effective δ_{VCL} is much smaller than the worst-case bound, i.e., $\delta_{VCL} \leq \tau \log \frac{1}{\alpha_{\min}} \ll \Delta$.

Generalization Bound for Vector Contrastive Learning

Recalling the generalization error bound for any $f \in \mathcal{F}$ in Equ.15, we substitute the improved local dispersion bound δ_{VCL} for δ in the vector CL case and use the fact in Equ.24, so that we will obtain:

$$R_{VCL}(f) \leq \hat{R}(f) + 2 \left(\frac{\tau \log \frac{1}{\alpha_{\min}}}{\Delta} \right) \mathfrak{R}_n(\mathcal{F}) + O\left(\sqrt{\frac{\log(1/\varepsilon)}{nN}}\right) \quad (25)$$

Since typically $\tau \log(1/\alpha_{\min}) \ll \Delta$ (because the normalization forces the weights to be spread across several pixels rather than concentrating on one), the factor $\frac{\tau \log \frac{1}{\alpha_{\min}}}{\Delta}$ is much smaller than 1. In contrast, in the binary CL setting, the worst-case dispersion is $\delta_{BCL} \approx \Delta$, leading to a much looser bound. Compared with the Equ.18, our vector CL making a tighter generalization bound.

B. Technical Details

B.1. Appearance transformation operation \mathcal{T}_{ap}

The appearance transformation operation \mathcal{T}_{ap} consists of random noise, blurring, contrast, brightness, and in-painting. Specifically,

1. For the random noise operation, it randomly generates Gaussian noise from the Gaussian distribution with $\mu = 0$ (mean) and $\sigma \in [0, 0.02]$ (variance), and adds it to the image.
2. For the random blurring, it performs random Gaussian blurring with $\mu = 0$ and $\sigma \in [0, 0.05]$ on the image.
3. For the random contrast, it performs multiplicative transformation with $(x - \bar{x}) * \gamma + \bar{x}$ on the images x , where the \bar{x} is the average value and the $\gamma \in [0.5, 1.5]$ is the scaling value.
4. For the random brightness, it performs additive transformation with $x + \beta$ on the images, where the β is randomly sampled from a Gaussian distribution with $\mu = 0$ and $\sigma \in [0, 0.1]$.
5. For the random in-painting, it randomly selects boxes, and the contents of these regions are replaced by the noise from a uniform distribution.

These five sub-operations are used sequentially with a probability of 0.9 for the image with appearance transformation.

B.2. Space transformation operation \mathcal{T}_{sp}

We utilize random affine transformation [5] to construct the space transformation operation \mathcal{T}_{sp} . For a clearer illustration, we introduce it in 2D situation. As shown in Equ.26, it as four sub-operations including the translation $t_x, t_y \in [-0.2, 0.2]$, rotation $\theta \in [-\pi/9, \pi/9]$, shearing $sh_x, sh_y \in [-\pi/32, \pi/32]$, and scaling $s_x, s_y \in [0.5, 1.5]$, where the H, W in the Equ.26 are the height and width of the medical images. These operations are These operations form an affine transformation matrix ϕ_{ab} that transforms the position of each pixel \mathbf{p}_a in the image to a new position \mathbf{p}_{ab} . Therefore, the ground truth vector v_{ab}^i will be generated via the coordinate difference on the image grid $v_{ab}^i = \mathbf{p}_{ab}^i - \mathbf{p}_a^i$, and the vectors at each position jointly construct the displacement vector field (DVF) $\psi_{ab} = \{v_{ab}^i\}_{i \in \mathbb{R}}$. The space-transformed view x_b is generated by the DVF ψ_{ab} via moving the pixels to target positions and completing the non-integer coordinates by bilinear interpolation.

B.3. Mask ϵ_{ab} indicates matched regions

The mask ϵ_{ab} eliminates the content mismatch of two views x_a, x_b caused by the spatial transformation. It is calculated from the DVF ψ_{ab} according to whether the transformed coordinates exceed the image grid. For each position i on image grid, the value of the ϵ_{ab}^i is

$$\epsilon_{ab}^i = \mathbf{1}_{(0,H)}(v_x^i + p_x^i) \wedge \mathbf{1}_{(0,W)}(v_y^i + p_y^i), \quad (27)$$

where the $\mathbf{1}_{(0,H)}(\cdot)$ and $\mathbf{1}_{(0,W)}(\cdot)$ are Iverson Notation [34]. Therefore, the mask ϵ_{ab} be generated whose 0 values indicate the mismatched regions and 1 values indicate the matched regions.

B.4. Multi-scale fusion operation \odot in our VPA

The fusion operation \odot in our vector pyramid aggregation integrates the DVFs from different levels. Here, we utilize the fusion of DVFs in level 0 ψ_{ab}^0 and level 1 ψ_{ab}^1 to introduce this operation. It has three steps: **1) Scale alignment:** The level 0 DVF ψ_{ab}^0 is up-sampled to the same size of level 1 DVF ψ_{ab}^1 via bilinear interpolation. Then the values are enlarged (double) to adapt to the size of the level 1 grid. **2) Space alignment:** To align the center coordinates of the vectors in these two level DVFs, the level 0 DVF is transformed to align the level 1 DVF. **3) Vector fusion:** Finally, the DVFs in two levels are fused via addition. The whole fusion operation \odot is formulated as,

$$\psi_{ab}^1 \odot \psi_{ab}^0 = \psi_{ab}^1 + \underbrace{\psi_{ab}^1 (2 * \mathcal{I}_{H \times W}(\psi_{ab}^0))}_{\text{Space alignment}}, \quad (28)$$

where H and W are the height and width of level 1 grid, and \mathcal{I} is the bilinear interpolation.

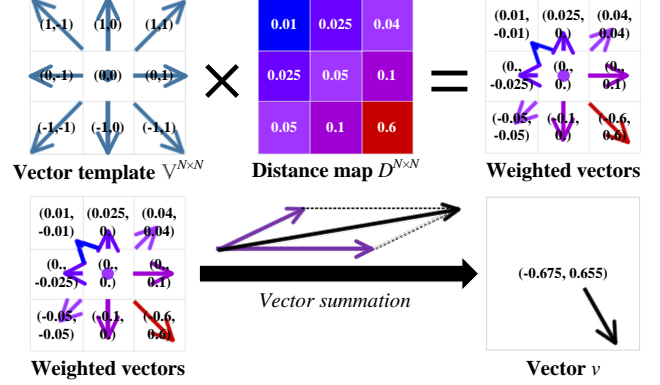


Figure 8. The details of our vector template matrix. It is multiplied to the distance map mapping the distances as vectors. The values in the distance map are examples.

B.5. Vector template $\nabla^{N \times N}$ maps distances as vector

The vector template matrix describes the basic spatial relationship of pixels that indicates the vectors in which the center coordinates pointing to the coordinates in the receptive field. As shown in Fig.8, for a clear illustration, we assume that the template is a 2D matrix (2 channels) with 3×3 receptive fields. The value in each position is the vector, i.e., (x, y) , that indicates the relative position offset from the center coordinate so that the $\nabla^{3 \times 3} = \{(x, y) | x, y \in \{-1, 0, 1\}\}$. To map the distances as vectors, the vector template matrix is multiplied by the distance map $D^{N \times N}$ of the receptive field corresponding to the center coordinate, i.e., $D^{3 \times 3} \cdot \nabla^{3 \times 3} = \{(x, y) | x = \nabla_{[0]}^{i,j} * D^{i,j}, y = \nabla_{[1]}^{i,j} * D^{i,j}, i, j \in \{0, 1, 2\}\}$, for weighted vectors in a matrix. Finally, these weighted vectors are summed for the vector $v = \sum_{i,j}^{j \in \{0, 1, 2\}} D^{i,j} \cdot \nabla^{i,j}$ indicating the correspondence between the center coordinate $(0, 0)$ and the coordinates in the field.

C. Experiment Details

C.1. Datasets

As shown in Tab.2, eight publicly available datasets are involved in this paper, specifically,

CANDI [36] The Child and Adolescent NeuroDevelopment Initiative (CANDI) dataset has 103 T1 brain MR volumes from 57 males and 46 females. Totally 28 brain tissue regions are annotated for masks. For the segmentation task (CANDI_S), 40, 20, and 43 volumes are used as training, validation, and test sets. Following [25], we resize and crop $160 \times 160 \times 128$ volumes on the brain regions, and then normalize the intensity via $\frac{x - \min(x)}{\max(x) - \min(x)}$.

FeTA21 [54] The Fetal Tissue Annotation 2021 (FeTA21) challenge dataset has 120 fetal T2w brain MR volumes, and 80 of them are available as the training data in the challenge. We split the 80 volumes and set 20 of them

$$\begin{aligned}
\phi_{ab} &= \overbrace{\begin{bmatrix} 1 & 0 & t_x H \\ 0 & 1 & t_y W \\ 0 & 0 & 1 \end{bmatrix}}^{\text{Translation}} \overbrace{\begin{bmatrix} \cos \theta & -\sin \theta & 0 \\ \sin \theta & \cos \theta & 0 \\ 0 & 0 & 1 \end{bmatrix}}^{\text{Rotation}} \overbrace{\begin{bmatrix} 1 & sh_x & 0 \\ sh_y & 1 & 0 \\ 0 & 0 & 1 \end{bmatrix}}^{\text{Shearing}} \overbrace{\begin{bmatrix} s_x & 0 & 0 \\ 0 & s_y & 0 \\ 0 & 0 & 1 \end{bmatrix}}^{\text{Scaling}} = \begin{bmatrix} a_{11} & a_{12} & t_x H \\ a_{21} & a_{22} & t_y W \\ 0 & 0 & 1 \end{bmatrix} \\
&= \begin{bmatrix} s_x \cos \theta + sh_x s_y \sin \theta & -s_x \sin \theta + sh_x s_y \cos \theta & t_x H \\ sh_y s_x \cos \theta & -sh_y s_x \sin \theta + s_y \cos \theta & t_y W \\ 0 & 0 & 1 \end{bmatrix}, \\
v_{ab}^i &= \mathbf{P}_{ab}^i - \mathbf{P}_a^i = \phi_{ab} \cdot \begin{bmatrix} p_x^i \\ p_y^i \\ 1 \end{bmatrix} - \begin{bmatrix} p_x^i \\ p_y^i \\ 1 \end{bmatrix} = \begin{bmatrix} (a_{11} - 1)p_x^i + a_{12}p_y^i + t_x H \\ a_{21}p_x^i + (a_{22} - 1)p_y^i + t_y W \\ 1 \end{bmatrix} = \begin{bmatrix} v_x^i \\ v_y^i \\ 1 \end{bmatrix}, \psi_{ab} = \{v_{ab}^i\}_{i \in \mathbb{R}}
\end{aligned} \tag{26}$$

Dataset	Type	Num	D	P	Task
CANDI [36]	3D T1 brain MRI	103	✓		S
FeTA21 [54]	3D T2 brain MRI	80	✓		S
SCR [68]	2D chest X-ray	247	✓		S
KiPA22 [24]	3D kidney CT	130	✓		S
FIVES [35]	2D fundus	800	✓		S
PDCXR [37]	2D chest X-ray	5,956	✓		C
STOIC [57]	3D chest CT	2,000	✓		C
ChestX-ray8 [75]	2D chest X-ray	112,120		✓	-
PPMI (T1) [45]	3D T1 brain MRI	837		✓	-

Table 2. A Total of 9 publicly available datasets are involved in this paper for the experiments, achieving great reproducibility. The “D” and “P” mean the datasets are used for downstream tasks and pretraining tasks. The “S” and “C” are the segmentation and classification tasks.

as the training set, 20 of them as the validation set, and 40 of them as test set. We normalize the intensity of the images via $\frac{x - \min(x)}{\max(x) - \min(x)}$ and use the $128 \times 128 \times 128$ random cropping to unify the input size.

SCR [68] The segmentation of chest radiographs (SCR) dataset is from the JSRT database [61] with 247 2048 \times 2048 posterior to anterior (PA) chest radiographs. Three chest-related structures, including the heart, chest, and clavicle, are annotated for masks. We set 100 of them as the training set, 47 of them as a validation set, and 100 of them as the test set. Following [25], we resize the images to 512 \times 512, and normalize the intensity via $x/255$ for the segmentation task (SCR_S).

KiPA22 [24] The kidney parsing 2022 (KiPA22) challenge dataset has 130 kidney CT volumes. These images are cropped from 130 abdominal CT angiography volumes for kidney regions with tumors. Four kidney-related structures, including the kidney, vessel, vein, and tumor, are annotated for masks. In 2D evaluation (KiPA_S^{2D}), 13,846 2D slices from 70 volumes are used as the training set, 5,864 2D slices from 30 volumes are used as the validation set, 5,959 2D slices from 30 volumes are used as the test set. We normalize the intensity of the images via $\frac{\max(\min(0,x),2048)}{2048}$, and use the 128×128 randomly to unify the input size. For 3D evaluation (KiPA_S^{3D}), 70, 30, and 30 volumes are

used as training, validation, and test sets. We normalize the intensity of the images via $\frac{\max(\min(0,x),2048)}{2048}$, and use the $128 \times 128 \times 128$ randomly to unify the input size.

FIVES [35] The fundus image vessel segmentation (FIVES) dataset consists of 800 color fundus photographs with vessel annotation from 573 patients. 540, 60, and 200 of the images are used as training, validation, and test sets. We resize the images to 512 \times 512, and normalize the intensity via $x/255$ for the segmentation task (FIVES_S).

PDCXR [37] The pneumonia Detection Using Chest X-ray (PDCXR) dataset has 5,856 chest X-ray images for the diagnosis of pneumonia. Following [37], 3,659 of them are used as training set (2,714 pneumonia, 945 normal), 1,573 of them are used as validation set (1,169 pneumonia, 404 normal), and 624 of them are used as test set (390 pneumonia, 234 normal). We resize the images to 512 \times 512, and normalize the intensity via $x/255$ for classification task (PDCXR_C).

STOIC [57] The STOIC dataset is from the STOIC 2021 challenge with 2000 chest CT volumes for COVID-19 diagnosis. Following [26], 1000 of them are used as training set (603 COVID-19, 397 normal), 400 of them are used as validation set (241 COVID-19, 159 normal), and 600 of them are used as test set (361 COVID-19, 239 normal). We utilize the Lungmask [32] to extract the lung regions avoiding the interference of the background, resample the resolutions to 1mm³, and normalize the intensity via $\frac{\max(\min(0,x),2048)}{2048}$ for classification task (STOIC_C).

ChestX-ray8 [75] The ChestX-ray8 is our pre-training dataset in 2D evaluation. It has 112,120 frontal-view chest X-ray images with 1024 \times 1024 resolution. 44,810 of them are scanned from the anterior to posterior (AP) view and 67,310 of them are scanned from the PA view. We resize the images to 512 \times 512, and normalize the intensity $x/255$. During the pre-training, 384 \times 384 patches are randomly cropped for augmentation.

PPMI [45] The PPMI is our pre-training dataset in 3D evaluation. It is extracted from the PPMI database which is a large Parkinson progression marker initiative database, for

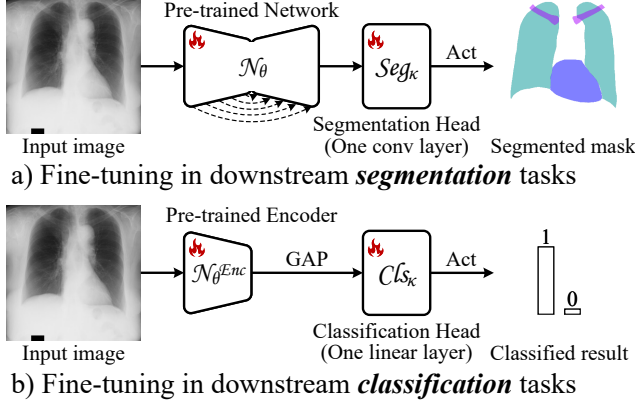


Figure 9. The detailed implementations in our downstream tasks, including the a) segmentation and b) classification.

837 T1 brain MR volumes. Following the pre-processing in the CANIA dataset, we resize and crop $160 \times 160 \times 128$ volumes on the brain regions, and then normalize the intensity via $\frac{x - \min(x)}{\max(x) - \min(x)}$. We also extract the brain regions via HD-BET [33] to avoid the interference of background. During the pre-training, $128 \times 128 \times 128$ patches are randomly cropped for augmentation.

C.2. Implementations

Our experiments are implemented by PyTorch [52] which is a widely recognized deep learning library on NVIDIA A100 SXUM4 GPU with 40 GB memory. Specifically,

C.2.1. Pre-training implementation

In both 2D evaluation and 3D evaluation, we utilize the Adam optimizer [38] with the learning rate of 1×10^{-4} and iterations of 2×10^5 . For 2D evaluation, 24 2D chest X-ray images from ChestX-ray8 [75] dataset are randomly sampled as a batch in each iteration with 384×384 random cropping augmentation. For 3D evaluation, 2 3D brain MR volumes from the PPMI [45] dataset are randomly sampled as a batch in each iteration with $128 \times 128 \times 128$ random cropping augmentation.

C.2.2. Downstream implementation

As shown in Fig.9, following [26], we utilize the fine-tuning evaluation to demonstrate the adaptation ability in downstream tasks. The gradient optimizes all parameters through the frameworks during the training. All the downstream tasks are trained by Adam optimizer [38] with the learning rate of 1×10^{-4} and iterations of 4×10^4 .

For segmentation tasks, the whole pre-trained network \mathcal{N}_θ is utilized to extract the pixel-wise features (level 4) f^4 , and these features are putted into a new segmentation head Seg_κ to predict the final segmentation masks. The segmentation head is a convolutional layer to map the features to the channels of segmentation targets, thus constructing a segmentation framework for the SCR_S , $KiPA22_S^{2D}$, $FIVES_S$,

Backbone	Methods	$SCR_S^{25\%}$	$PDCXR_C$	$KiPA22_S^{2D}$	$FIVES_S$	AVG
U-Net [59]	Scratch	81.8	90.4	74.1	79.4	81.4
	COVER	94.0(+12.2)	95.9(+5.5)	80.0(+5.9)	87.2(+7.8)	89.3(+7.9)
TransUNet [9]	Scratch	89.2	77.4	57.6	81.7	76.5
	COVER	93.4(+4.2)	90.6(+13.2)	76.7(+19.1)	86.5(+4.8)	86.8(+10.3)
SwinUNet [6]	Scratch	85.6	93.0	69.1	77.0	81.2
	COVER	86.9(+1.3)	95.6(+2.6)	72.6(+3.5)	84.8(+7.8)	85.0(+3.8)
U-KAN [41]	Scratch	89.4	89.3	61.3	80.3	80.1
	COVER	93.8(+4.4)	95.6(+6.3)	71.8(+10.5)	84.9(+4.6)	86.5(+6.4)

Table 3. Our COVER has great cross-architecture compatibility that achieves significant improvement on all U-Net, TransUNet, SwinUNet, and UKAN. We evaluate it in our 2D setting.

$SCR_S^{25\%}$		$PDCXR_C$		$KiPA22_S^{2D}$		$FIVES_S$		AVG	
Cor \uparrow	$p \downarrow$	Cor \uparrow	$p \downarrow$	Cor \uparrow	$p \downarrow$	Cor \uparrow	$p \downarrow$	Cor \uparrow	$p \downarrow$
0.908	< 0.001	0.898	< 0.001	0.949	< 0.001	0.995	< 0.001	0.938	< 0.001

Table 4. The test-retest reliability analysis [20] of our COVER on the tasks of 2D evaluation. The *Cor* is the Pearson correlation coefficient [14], and the *p* is the p-value.

$CANDI_S$, and $KiPA22_S^{3D}$ tasks. We use the sum of Dice loss [84] and cross-entropy loss [44] between the predicted masks and ground truths to train the segmentation tasks.

For classification tasks, the encoder part of the pre-trained network \mathcal{N}_θ^{Enc} is utilized to extract the high-level features (level 0) f^0 , and a global adaptive pooling is used to compress features. Then these compressed features are putted into a classification head Cls_κ to achieve the classified results, thus constructing a segmentation framework for the $PDCXR_C$ and $STOIC_C$ tasks. We utilize the cross-entropy loss [44] between the predicted categories and ground truths to train the classification.

D. More Framework Analysis and Results

D.1. Analysis of the reliability

As shown in Tab.4, we utilize the test-retest analysis [20] to evaluate the reliability of our COVER. We pre-trained and adapted our method twice in our 2D evaluation from different initialization states, and then calculated the correlation coefficient [14] and p-value between these two results. Our COVER achieved 0.938 average Cors over four tasks demonstrating very high consistency between two training sessions. All p-values lower than 0.001 illustrated the significant consistency. Therefore, these results show our powerful reliability across initialization states, supporting the implementation in the application.

D.2. Analysis of cross-architecture compatibility

As shown in Tab.3, our COVER has great cross-architecture compatibility that achieves significant improvement on all U-Net [59] (CNN-based), TransUNet [9] (CNN-Transformer-based), SwinUNet [6] (Transformer-based), and UKAN [41] (KAN-based). We utilize these four networks with different paradigms as the backbone network in our COVER framework and train the framework on our 2D evaluation setting. Compared with the “scratch” on these networks, our COVER has achieved more than 3% average improvement owing to the learned knowledge from the pre-



Figure 10. The analysis of the pre-training data amount. When enlarging the pre-training data amount, the performance of our COVER is improved gradually.

training data. Especially, on the TransUNet which utilizes a vision transformer and is easy to fall into an over-fitting state, our COVER brings a significant 10.3% average improvement.

D.3. Analysis pre-training data amount

As shown in Fig.10, we evaluate the variation of our COVER’s performance with the enlarging of the pre-training data amount on our 2D evaluation and adapt the pre-trained model to the $SCR_S^{25\%}$ via linear evaluation. Compared with the “scratch”, our COVER will bring a significant improvement even though only 25% pre-training data is involved. When further enlarging the -pre-training dataset, the gain of performance gradually decreases owing to the similarity of the same category of medical images in the pre-training dataset. Fortunately, our COVER has a powerful modeling ability for pixel-wise features, enabling the learning from the details effectively, so the performance of the model is still improving gradually.

D.4. Visualization of the segmentation results

The visualization of the segmentation results (Fig.11) demonstrates our superiority in the adaptation of pixel-wise tasks. Due to our vector CL with distance modeling, the pre-training enables the networks pixel-wise representation with controllable dispersion. It has two observations: 1) For large objects with varied appearances like the tumors in $KiPA22_S^{2D}$ and $KiPA22_S^{3D}$, our COVER achieves excellent integrity owing to its disentanglement of underlying explanatory factors hidden in low-level sensory data. The BYOL, SimSiam, Model Genesis, Rotation, and “Scratch” have poor performance on the tumors, because of their lack of modeling for distinct features. 2) For small objects like the thin vessels in $FIVE_S$, small brain tissues in $CANDI_S$ and $FeTA21_S$, and clavicles in $SCR_S^{25\%}$, our COVER also has fine segmentation owing to our pixel-wise representation with distance modeling. Such representation preserves the distinction of detail features thus making the networks easy to segment these regions in downstream tasks.

D.5. Visualization of multi-scale vectors

We visualize more results of our regressed multi-scale vectors (corresponding to Fig.8 in the manuscript) in Fig.12. It aligns the appearance-transformed view x_a to the space-transformed view x_b via the deformation of regressed vectors in different scale levels. In a large number of cases,

we can find that our VPA effectively aligns the regions with the same semantics between the views, illustrating that the regressed vectors are able to indicate the correspondence of the same semantics. Therefore, this means that in the embedding space, our vector CL can model closer distances between the same semantic objects and farther distances between different semantic objects, thus enabling our COVER to discover accurate correspondence in the receptive field.

References

- [1] Guha Balakrishnan, Amy Zhao, Mert R Sabuncu, John Guttag, and Adrian V Dalca. Voxelmorph: a learning framework for deformable medical image registration. *IEEE transactions on medical imaging*, 38(8):1788–1800, 2019. 3
- [2] Peter L Bartlett and Shahar Mendelson. Rademacher and gaussian complexities: Risk bounds and structural results. *Journal of Machine Learning Research*, 3(Nov):463–482, 2002. 9
- [3] Yoshua Bengio, Aaron Courville, and Pascal Vincent. Representation learning: A review and new perspectives. *IEEE transactions on pattern analysis and machine intelligence*, 35(8):1798–1828, 2013. 2, 3, 7
- [4] Rishi Bommasani, Drew A Hudson, Ehsan Adeli, Russ Altman, Simran Arora, Sydney von Arx, Michael S Bernstein, Jeannette Bohg, Antoine Bosselut, Emma Brunskill, et al. On the opportunities and risks of foundation models. *arXiv preprint arXiv:2108.07258*, 2021. 2
- [5] Lisa Gottesfeld Brown. A survey of image registration techniques. *ACM computing surveys (CSUR)*, 24(4):325–376, 1992. 11
- [6] Hu Cao, Yueyue Wang, Joy Chen, Dongsheng Jiang, Xi-aopeng Zhang, Qi Tian, and Manning Wang. Swin-unet: Unet-like pure transformer for medical image segmentation. In *European conference on computer vision*, pages 205–218. Springer, 2022. 13
- [7] Mathilde Caron, Piotr Bojanowski, Armand Joulin, and Matthijs Douze. Deep clustering for unsupervised learning of visual features. In *European Conference on Computer Vision*, 2018. 1, 3, 6, 9
- [8] Krishna Chaitanya, Ertunc Erdil, Neerav Karani, and Ender Konukoglu. Contrastive learning of global and local features for medical image segmentation with limited annotations. *Advances in neural information processing systems*, 33:12546–12558, 2020. 1, 6
- [9] Jieneng Chen, Jieru Mei, Xianhang Li, Yongyi Lu, Qihang Yu, Qingyue Wei, Xiangde Luo, Yutong Xie, Ehsan Adeli, Yan Wang, et al. Transunet: Rethinking the u-net architecture design for medical image segmentation through the lens of transformers. *Medical Image Analysis*, 97:103280, 2024. 13
- [10] Richard J Chen, Tong Ding, Ming Y Lu, Drew FK Williamson, Guillaume Jaume, Andrew H Song, Bowen Chen, Andrew Zhang, Daniel Shao, Muhammad Shaban, et al. Towards a general-purpose foundation model for computational pathology. *Nature Medicine*, 30(3):850–862, 2024. 1, 3

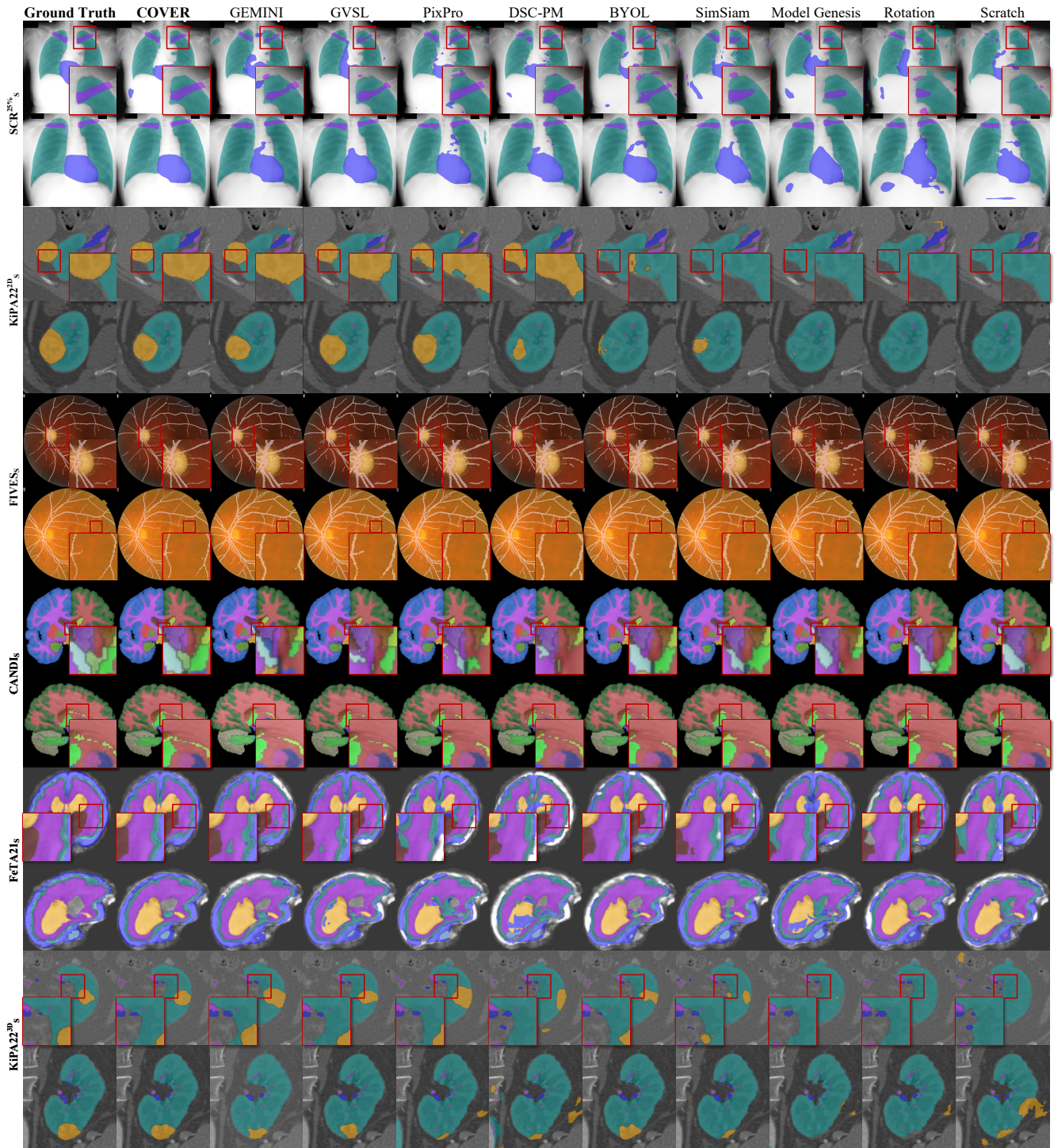


Figure 11. The visualization of the segmentation results for the methods with the top 2 average scores in each type. Our COVER achieves excellent integrity and fine segmentation ability for thin structures owing to its effective representation of pixel-wise features.

[11] Ting Chen, Simon Kornblith, Mohammad Norouzi, and Geoffrey Hinton. A simple framework for contrastive learning of visual representations. In *International conference on machine learning*, pages 1597–1607. PMLR, 2020. 1, 3, 6, 9

[12] Xinlei Chen and Kaiming He. Exploring simple siamese

representation learning. In *Proceedings of the IEEE/CVF Conference on Computer Vision and Pattern Recognition (CVPR)*, pages 15750–15758, 2021. 3, 6

[13] Xinlei Chen, Haoqi Fan, Ross Girshick, and Kaiming He. Improved baselines with momentum contrastive learning.

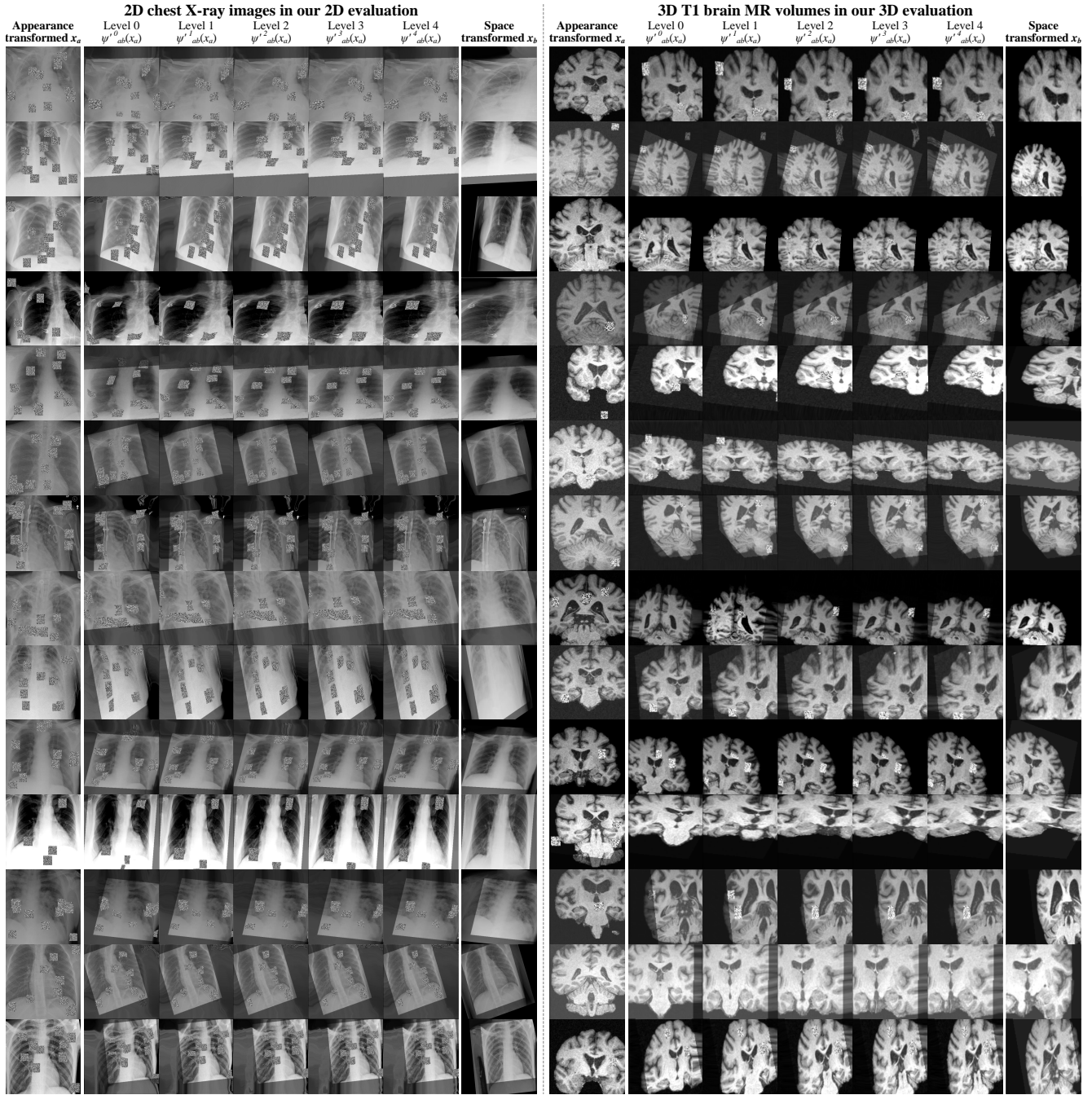


Figure 12. **Extension of multi-scale vectors analysis** (Fig.8 in manuscript): The visualization of the regressed vectors via the alignment of two views. Our VPA is able to discover the correspondence of the semantics at multiple levels for both global and detailed representation.

arXiv preprint arXiv:2003.04297, 2020. 1, 6, 9

- [14] Israel Cohen, Yiteng Huang, Jingdong Chen, Jacob Benesty, Jacob Benesty, Jingdong Chen, Yiteng Huang, and Israel Cohen. Pearson correlation coefficient. *Noise reduction in speech processing*, pages 1–4, 2009. 13
- [15] Oliver Contier, Chris I Baker, and Martin N Hebart. Distributed representations of behaviour-derived object dimensions in the human visual system. *Nature Human Behaviour*, 8(11):2179–2193, 2024. 3

- [16] Qiaole Dong, Chenjie Cao, and Yanwei Fu. Rethinking optical flow from geometric matching consistent perspective. In *Proceedings of the IEEE/CVF Conference on Computer Vision and Pattern Recognition*, pages 1337–1347, 2023. 3
- [17] Viktoria Ehm, Maolin Gao, Paul Roetzer, Marvin Eisenberger, Daniel Cremers, and Florian Bernard. Partial-to-partial shape matching with geometric consistency. In *Proceedings of the IEEE/CVF Conference on Computer Vision and Pattern Recognition*, pages 27488–27497, 2024. 3

- [18] Rafael C Gonzales and Paul Wintz. *Digital image processing*. Addison-Wesley Longman Publishing Co., Inc., 1987. 1
- [19] Jean-Bastien Grill, Florian Strub, Florent Altché, Corentin Tallec, Pierre Richemond, Elena Buchatskaya, Carl Doersch, Bernardo Pires, Zhaohan Guo, Mohammad Azar, et al. Bootstrap your own latent: A new approach to self-supervised learning. In *Neural Information Processing Systems*, 2020. 1, 3, 6, 9
- [20] Louis Guttman. A basis for analyzing test-retest reliability. *Psychometrika*, 10(4):255–282, 1945. 13
- [21] Fatemeh Haghighi, Mohammad Reza Hosseinzadeh Taher, Michael B Gotway, and Jianming Liang. Self-supervised learning for medical image analysis: Discriminative, restorative, or adversarial? *Medical Image Analysis*, 94:103086, 2024. 1
- [22] Kaiming He, Haoqi Fan, Yuxin Wu, Saining Xie, and Ross Girshick. Momentum contrast for unsupervised visual representation learning. In *Proceedings of the IEEE/CVF conference on computer vision and pattern recognition*, pages 9729–9738, 2020. 1, 3
- [23] Yuting He, Tiantian Li, Rongjun Ge, Jian Yang, Youyong Kong, Jian Zhu, Huazhong Shu, Guanyu Yang, and Shuo Li. Few-shot learning for deformable medical image registration with perception-correspondence decoupling and reverse teaching. *IEEE Journal of Biomedical and Health Informatics*, 26(3):1177–1187, 2021. 3
- [24] Yuting He, Guanyu Yang, Jian Yang, Rongjun Ge, Youyong Kong, Xiaomei Zhu, Shaobo Zhang, Pengfei Shao, Huazhong Shu, Jean-Louis Dillenseger, et al. Meta grayscale adaptive network for 3d integrated renal structures segmentation. *Medical Image Analysis*, 71:102055, 2021. 6, 12
- [25] Yuting He, Rongjun Ge, Xiaoming Qi, Yang Chen, Jiasong Wu, Jean-Louis Coatrieux, Guanyu Yang, and Shuo Li. Learning better registration to learn better few-shot medical image segmentation: Authenticity, diversity, and robustness. *IEEE Transactions on Neural Networks and Learning Systems*, 35(2):2588–2601, 2022. 11, 12
- [26] Yuting He, Guanyu Yang, Rongjun Ge, Yang Chen, Jean-Louis Coatrieux, Boyu Wang, and Shuo Li. Geometric visual similarity learning in 3d medical image self-supervised pre-training. In *Proceedings of the IEEE/CVF Conference on Computer Vision and Pattern Recognition (CVPR)*, 2023. 2, 3, 5, 6, 12, 13
- [27] Yuting He, Rongjun Ge, Xiaoming Qi, Yang Chen, Jiasong Wu, Jean-Louis Coatrieux, Guanyu Yang, and Shuo Li. Learning better registration to learn better few-shot medical image segmentation: Authenticity, diversity, and robustness. *IEEE Transactions on Neural Networks and Learning Systems*, 35(2):2588–2601, 2024. 3
- [28] Yuting He, Fuxiang Huang, Xinrui Jiang, Yuxiang Nie, Minghao Wang, Jiguang Wang, and Hao Chen. Foundation model for advancing healthcare: Challenges, opportunities, and future directions. *arXiv preprint arXiv:2404.03264*, 2024. 1, 3, 9
- [29] Yuting He, Boyu Wang, Rongjun Ge, Yang Chen, Guanyu Yang, and Shuo Li. Homeomorphism prior for false positive and negative problem in medical image dense contrastive representation learning, 2025. 2, 3, 5, 6
- [30] John Hinde and Clarice GB Demétrio. Overdispersion: models and estimation. *Computational statistics & data analysis*, 27(2):151–170, 1998. 1
- [31] Elad Hoffer and Nir Ailon. Deep metric learning using triplet network. In *Similarity-based pattern recognition: third international workshop, SIMBAD 2015, Copenhagen, Denmark, October 12–14, 2015. Proceedings 3*, pages 84–92. Springer, 2015. 3
- [32] Johannes Hofmanninger, Florian Prayer, Jeanny Pan, Sebastian Röhrich, Helmut Prosch, and Georg Langs. Automatic lung segmentation in routine imaging is primarily a data diversity problem, not a methodology problem. *European Radiology Experimental*, 4:1–13, 2020. 12
- [33] Fabian Isensee, Marianne Schell, Irada Pfueger, Gianluca Brugnara, David Bonekamp, Ulf Neuberger, Antje Wick, Heinz-Peter Schlemmer, Sabine Heiland, Wolfgang Wick, et al. Automated brain extraction of multisequence mri using artificial neural networks. *Human brain mapping*, 40(17):4952–4964, 2019. 13
- [34] Kenneth E Iverson. A programming language. In *Proceedings of the May 1–3, 1962, spring joint computer conference*, pages 345–351, 1962. 11
- [35] Kai Jin, Xingru Huang, Jingxing Zhou, Yunxiang Li, Yan Yan, Yibao Sun, Qianni Zhang, Yaqi Wang, and Juan Ye. Fives: A fundus image dataset for artificial intelligence based vessel segmentation. *Scientific data*, 9(1):475, 2022. 6, 12
- [36] David N Kennedy, Christian Haselgrove, Steven M Hodge, Pallavi S Rane, Nikos Makris, and Jean A Frazier. Candishare: A resource for pediatric neuroimaging data. *Neuroinformatics*, 10(3):319, 2012. 6, 11, 12
- [37] Daniel S Kermany, Michael Goldbaum, Wenjia Cai, Carolina CS Valentim, Huiying Liang, Sally L Baxter, Alex McKeown, Ge Yang, Xiaokang Wu, Fangbing Yan, et al. Identifying medical diagnoses and treatable diseases by image-based deep learning. *cell*, 172(5):1122–1131, 2018. 6, 12
- [38] Diederik P Kingma and Jimmy Ba. Adam: A method for stochastic optimization. *arXiv preprint arXiv:1412.6980*, 2014. 13
- [39] Vladimir Koltchinskii. Local rademacher complexities and oracle inequalities in risk minimization. 2006. 9
- [40] Nikos Komodakis and Spyros Gidaris. Unsupervised representation learning by predicting image rotations. In *International Conference on Learning Representations (ICLR)*, 2018. 3, 6
- [41] Chenxin Li, Xinyu Liu, Wuyang Li, Cheng Wang, Hengyu Liu, and Yixuan Yuan. U-kan makes strong backbone for medical image segmentation and generation. *arXiv preprint*, 2024. 13
- [42] Xiaoni Li, Yu Zhou, Yifei Zhang, Aoting Zhang, Wei Wang, Ning Jiang, Haiying Wu, and Weiping Wang. Dense semantic contrast for self-supervised visual representation learning. In *Proceedings of the 29th ACM International Conference on Multimedia*, pages 1368–1376, 2021. 1, 2, 3, 5, 6
- [43] Siladitya Manna, Saumik Bhattacharya, and Umпада Pal. Self-supervised visual representation learning for medical

- image analysis: A comprehensive survey. *Transactions on Machine Learning Research*. 1, 3
- [44] Anqi Mao, Mehryar Mohri, and Yutao Zhong. Cross-entropy loss functions: Theoretical analysis and applications. In *International conference on Machine learning*, pages 23803–23828. PMLR, 2023. 13
- [45] Kenneth Marek, Danna Jennings, Shirley Lasch, Andrew Siderowf, Caroline Tanner, Tanya Simuni, Chris Coffey, Karl Kiebertz, Emily Flagg, Sohini Chowdhury, et al. The parkinson progression marker initiative (ppmi). *Progress in neurobiology*, 95(4):629–635, 2011. 6, 12, 13
- [46] Mehryar Mohri. *Foundations of machine learning*, 2018. 4, 9
- [47] Michael Moor, Oishi Banerjee, Zahra Shakeri Hossein Abad, Harlan M Krumholz, Jure Leskovec, Eric J Topol, and Pranav Rajpurkar. Foundation models for generalist medical artificial intelligence. *Nature*, 616(7956):259–265, 2023. 1, 3
- [48] Frank H Netter. *Atlas of human anatomy, Professional Edition E-Book: including NetterReference. com Access with full downloadable image Bank*. Elsevier health sciences, 2014. 1
- [49] Pedro O O Pinheiro, Amjad Almahairi, Ryan Benmalek, Florian Golemo, and Aaron C Courville. Unsupervised learning of dense visual representations. *Advances in Neural Information Processing Systems*, 33:4489–4500, 2020. 6
- [50] Aaron van den Oord, Yazhe Li, and Oriol Vinyals. Representation learning with contrastive predictive coding. *arXiv preprint arXiv:1807.03748*, 2018. 1, 9
- [51] Maxime Oquab, Timothée Darcet, Théo Moutakanni, Huy Vo, Marc Szafraniec, Vasil Khalidov, Pierre Fernandez, Daniel Haziza, Francisco Massa, Alaaeldin El-Nouby, et al. Dinov2: Learning robust visual features without supervision. *Transactions on Machine Learning Research Journal*, pages 1–31, 2024. 1, 3, 9
- [52] Adam Paszke, Sam Gross, Francisco Massa, Adam Lerer, James Bradbury, Gregory Chanan, Trevor Killeen, Zeming Lin, Natalia Gimelshein, Luca Antiga, et al. Pytorch: An imperative style, high-performance deep learning library. *Advances in neural information processing systems*, 32, 2019. 13
- [53] Deepak Pathak, Philipp Krahenbuhl, Jeff Donahue, Trevor Darrell, and Alexei A Efros. Context encoders: Feature learning by inpainting. In *Proceedings of the IEEE conference on computer vision and pattern recognition*, pages 2536–2544, 2016. 3, 6
- [54] Kelly Payette, Hongwei Bran Li, Priscille de Dumast, Roxane Licandro, Hui Ji, Md Mahfuzur Rahman Siddiquee, Daguang Xu, Andriy Myronenko, Hao Liu, Yuchen Pei, et al. Fetal brain tissue annotation and segmentation challenge results. *Medical image analysis*, 88:102833, 2023. 6, 11, 12
- [55] Guangzhi Qu, Salim Hariri, and Mazin Yousif. A new dependency and correlation analysis for features. *IEEE Transactions on Knowledge and Data Engineering*, 17(9):1199–1207, 2005. 2, 3, 4
- [56] Quan Quan, Qingsong Yao, Heqin Zhu, and S Kevin Zhou. Igu-aug: Information-guided unsupervised augmentation and pixel-wise contrastive learning for medical image analysis. *IEEE Transactions on Medical Imaging*, 2024. 1
- [57] Marie-Pierre Revel, Samia Boussouar, Constance de Margerie-Mellon, Inès Saab, Thibaut Lapotre, Dominique Mompoin, Guillaume Chassagnon, Audrey Milon, Mathieu Lederlin, Souhail Bennani, et al. Study of thoracic ct in covid-19: The stoic project. *Radiology*, 301(1):E361–E370, 2021. 6, 12
- [58] Ignacio Rocco, Relja Arandjelovic, and Josef Sivic. Convolutional neural network architecture for geometric matching. In *Proceedings of the IEEE conference on computer vision and pattern recognition*, pages 6148–6157, 2017. 3
- [59] Olaf Ronneberger, Philipp Fischer, and Thomas Brox. U-net: Convolutional networks for biomedical image segmentation. In *International Conference on Medical image computing and computer-assisted intervention*, pages 234–241. Springer, 2015. 6, 13
- [60] Nikunj Saunshi, Orestis Plevrakis, Sanjeev Arora, Mikhail Khodak, and Hrishikesh Khandeparkar. A theoretical analysis of contrastive unsupervised representation learning. In *International Conference on Machine Learning*, pages 5628–5637. PMLR, 2019. 1, 3
- [61] Junji Shiraishi, Shigehiko Katsuragawa, Junpei Ikezoe, Tsuneo Matsumoto, Takeshi Kobayashi, Ken-ichi Komatsu, Mitate Matsui, Hiroshi Fujita, Yoshie Kodera, and Kunio Doi. Development of a digital image database for chest radiographs with and without a lung nodule: receiver operating characteristic analysis of radiologists’ detection of pulmonary nodules. *American Journal of Roentgenology*, 174(1):71–74, 2000. 12
- [62] Kihyuk Sohn. Improved deep metric learning with multi-class n-pair loss objective. *Advances in neural information processing systems*, 29, 2016. 3
- [63] Juan Luis Suárez, Salvador García, and Francisco Herrera. A tutorial on distance metric learning: Mathematical foundations, algorithms, experimental analysis, prospects and challenges. *Neurocomputing*, 425:300–322, 2021. 2, 3
- [64] Abdel Aziz Taha and Allan Hanbury. Metrics for evaluating 3d medical image segmentation: analysis, selection, and tool. *BMC medical imaging*, 15(1):1–28, 2015. 6
- [65] Janine Thoma, Danda Pani Paudel, and Luc V Gool. Soft contrastive learning for visual localization. *Advances in Neural Information Processing Systems*, 33:11119–11130, 2020. 1
- [66] Yonglong Tian, Chen Sun, Ben Poole, Dilip Krishnan, Cordelia Schmid, and Phillip Isola. What makes for good views for contrastive learning? *Advances in Neural Information Processing Systems*, 33:6827–6839, 2020. 1, 3, 9
- [67] Laurens Van der Maaten and Geoffrey Hinton. Visualizing data using t-sne. *Journal of machine learning research*, 9(11), 2008. 8
- [68] Bram Van Ginneken, Mikkil B Stegmann, and Marco Loog. Segmentation of anatomical structures in chest radiographs using supervised methods: a comparative study on a public database. *Medical image analysis*, 10(1):19–40, 2006. 6, 12
- [69] A Vaswani. Attention is all you need. *Advances in Neural Information Processing Systems*, 2017. 5

- [70] Pascal Vincent, Hugo Larochelle, Isabelle Lajoie, Yoshua Bengio, Pierre-Antoine Manzagol, and Léon Bottou. Stacked denoising autoencoders: Learning useful representations in a deep network with a local denoising criterion. *Journal of machine learning research*, 11(12), 2010. 3, 6
- [71] Eugene Vorontsov, Alican Bozkurt, Adam Casson, George Shaikovski, Michal Zelechowski, Kristen Severson, Eric Zimmermann, James Hall, Neil Tenenholtz, Nicolo Fusi, et al. A foundation model for clinical-grade computational pathology and rare cancers detection. *Nature medicine*, pages 1–12, 2024. 1, 3
- [72] Feng Wang and Huaping Liu. Understanding the behaviour of contrastive loss. In *Proceedings of the IEEE/CVF conference on computer vision and pattern recognition*, pages 2495–2504, 2021. 1, 3
- [73] Haiqiao Wang, Dong Ni, and Yi Wang. Modet: Learning deformable image registration via motion decomposition transformer. In *International Conference on Medical Image Computing and Computer-Assisted Intervention*, pages 740–749. Springer, 2023. 3
- [74] Tongzhou Wang and Phillip Isola. Understanding contrastive representation learning through alignment and uniformity on the hypersphere. In *International conference on machine learning*, pages 9929–9939. PMLR, 2020. 1, 3
- [75] Xiaosong Wang, Yifan Peng, Le Lu, Zhiyong Lu, Mohammadhadi Bagheri, and Ronald M Summers. Chestx-ray8: Hospital-scale chest x-ray database and benchmarks on weakly-supervised classification and localization of common thorax diseases. In *Proceedings of the IEEE conference on computer vision and pattern recognition*, pages 2097–2106, 2017. 6, 12, 13
- [76] Xinlong Wang, Rufeng Zhang, Chunhua Shen, and Tao Kong. Densecl: A simple framework for self-supervised dense visual pre-training. *Visual Informatics*, 2022. 1, 2, 3, 5, 6
- [77] Zhaoqing Wang, Qiang Li, Guoxin Zhang, Pengfei Wan, Wen Zheng, Nannan Wang, Mingming Gong, and Tongliang Liu. Exploring set similarity for dense self-supervised representation learning. In *Proceedings of the IEEE/CVF Conference on Computer Vision and Pattern Recognition*, pages 16590–16599, 2022. 6
- [78] Linshan Wu, Jiaxin Zhuang, and Hao Chen. Large-scale 3d medical image pre-training with geometric context priors. *arXiv preprint arXiv:2410.09890*, 2024. 1, 3
- [79] Linshan Wu, Jiaxin Zhuang, and Hao Chen. Voco: A simple-yet-effective volume contrastive learning framework for 3d medical image analysis. In *Proceedings of the IEEE/CVF Conference on Computer Vision and Pattern Recognition*, pages 22873–22882, 2024. 1
- [80] Zhenda Xie, Yutong Lin, Zheng Zhang, Yue Cao, Stephen Lin, and Han Hu. Propagate yourself: Exploring pixel-level consistency for unsupervised visual representation learning. In *Proceedings of the IEEE/CVF Conference on Computer Vision and Pattern Recognition*, pages 16684–16693, 2021. 1, 2, 3, 5, 6
- [81] Ke Yan, Jinzheng Cai, Dakai Jin, Shun Miao, Dazhou Guo, Adam P Harrison, Youbao Tang, Jing Xiao, Jingjing Lu, and Le Lu. Sam: Self-supervised learning of pixel-wise anatomical embeddings in radiological images. *IEEE Transactions on Medical Imaging*, 41(10):2658–2669, 2022. 1
- [82] Liu Yang and Rong Jin. Distance metric learning: A comprehensive survey. *Michigan State University*, 2(2):4, 2006. 2, 3
- [83] Yi Zhang, Yiji Mao, Xuanyu Lu, Xingyu Zou, Hao Huang, Xinyang Li, Jiayue Li, and Haixian Zhang. From single to universal: tiny lesion detection in medical imaging. *Artificial Intelligence Review*, 57(8):192, 2024. 1
- [84] Rongjian Zhao, Buyue Qian, Xianli Zhang, Yang Li, Rong Wei, Yang Liu, and Yinggang Pan. Rethinking dice loss for medical image segmentation. In *2020 IEEE International Conference on Data Mining (ICDM)*, pages 851–860. IEEE, 2020. 13
- [85] Yukun Zhou, Mark A Chia, Siegfried K Wagner, Murat S Ayhan, Dominic J Williamson, Robbert R Struyven, Timing Liu, Moucheng Xu, Mateo G Lozano, Peter Woodward-Court, et al. A foundation model for generalizable disease detection from retinal images. *Nature*, 622(7981):156–163, 2023. 1, 3
- [86] Zongwei Zhou, Vatsal Sodha, Jiaxuan Pang, Michael B Gotway, and Jianming Liang. Models genesis. *Medical image analysis*, 67:101840, 2021. 3, 6
- [87] Jiuwen Zhu, Yuexiang Li, Yifan Hu, Kai Ma, S Kevin Zhou, and Yefeng Zheng. Rubik’s cube+: A self-supervised feature learning framework for 3d medical image analysis. *Medical image analysis*, 64:101746, 2020. 3